Department of Radio Science and Engineering

Dielectric rod waveguide components at sub-THz frequencies

Andrey Generalov

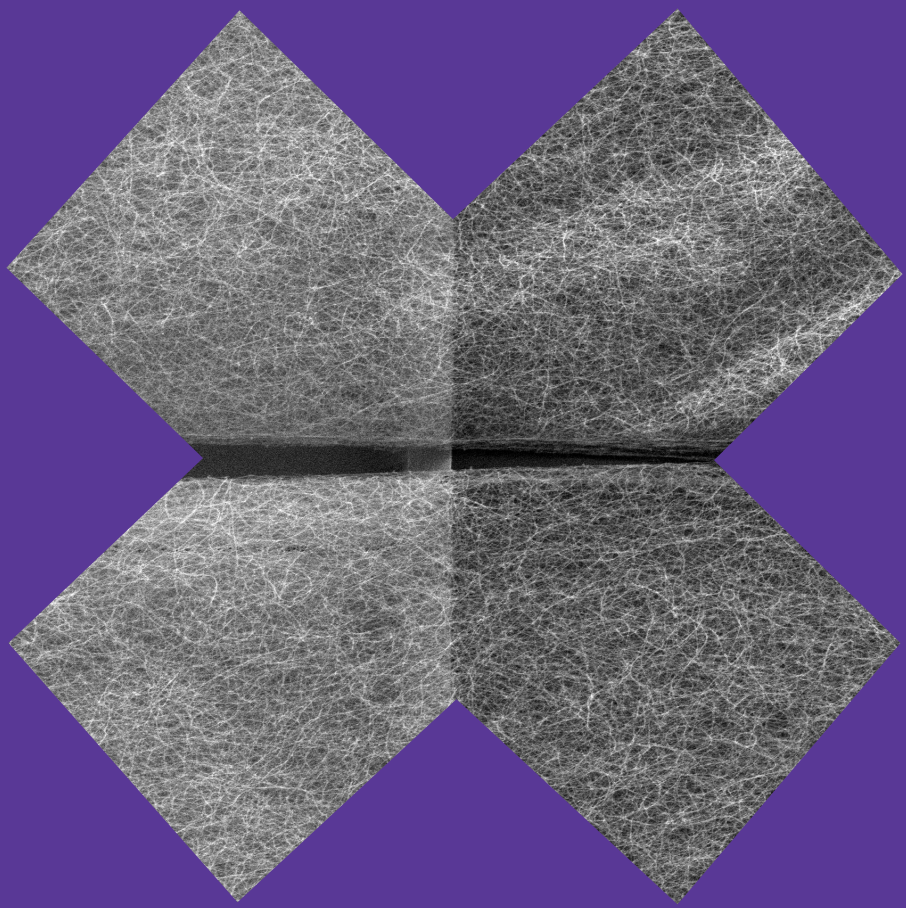

Aalto University

DOCTORAL DISSERTATIONS

Aalto University publication series
DOCTORAL DISSERTATIONS 99/2015

Dielectric rod waveguide components at sub-THz frequencies

Andrey Generalov

A doctoral dissertation completed for the degree of Doctor of Science (Technology) to be defended, with the permission of the Aalto University School of Electrical Engineering, at a public examination held at the lecture hall S1 of the school on 7 August 2014 at 12.

Aalto University
School of Electrical Engineering
Department of Radio Science and Engineering

Supervising professor
Professor Antti V. Räisänen

Thesis advisor
Dr. Juha A. Mallat, Dr. Dmitri V. Lioubtchenko

Preliminary examiners
Professor M. Himdi, University of Rennes 1, France
Dr. Panu Helistö, VTT Technical Research Centre of Finland

Opponent
Professor Yevhen Yashchyshyn, Warsaw University of Technology, Poland

Aalto University publication series
DOCTORAL DISSERTATIONS 99/2015

ISBN 978-952-60-6297-6 (printed)
ISBN 978-952-60-6298-3 (pdf)
ISSN-L 1799-4934
ISSN 1799-4934 (printed)
ISSN 1799-4942 (pdf)
http://urn.fi/URN:ISBN:978-952-60-6298-3

Unigrafia Oy
Helsinki 2015

Finland

441 697
Printed matter

Author
Andrey Generalov

Name of the doctoral dissertation
Dielectric rod waveguide components at sub-THz frequencies

Publisher School of Electrical Engineering

Unit Department of Radio Science and Engineering

Series Aalto University publication series DOCTORAL DISSERTATIONS 99/2015

Field of research Radio Engineering

Manuscript submitted 13 May 2015 **Date of the defence** 7 August 2015

Permission to publish granted (date) 9 July 2015 **Language** English

☐ **Monograph** ☒ **Article dissertation (summary + original articles)**

Abstract

This thesis is focused on the development of dielectric rod waveguide (DRW) components at sub-THz frequencies. DRWs proved themselves as low loss transmission lines at sub-millimeter wave and THz frequencies; they can be well matched with rectangular metal waveguides, and also used as antennas. In addition, the DRW allows integration of various components using standard microfabrication techniques, e.g. the bolometric power sensor can be integrated in the center of the DRW and measure the power travelling in the DRW, and a phase shifter based on a high impedance surface (HIS) can be manufactured on the surface of the DRW and can change the phase of the propagating wave inside the DRW.

In the first part of this thesis the narrow band and wide band DRW antennas were designed, manufactured and tested. The DRW antennas are lightweight, compact and easy to manufacture. The narrow band DRW antenna proved to operate in the range of 220 – 325 GHz. The wideband DRW antenna showed a constant performance over the band of 75 – 1100 GHz according to numerical simulations and over the band of 75 – 325 GHz experimentally. The radiation patterns of the antenna were measured in co- and cross-polarization. The co-polarization radiation patterns are nearly independent of frequency. The 3 dB beamwidth is 50° - 60°, and the 10 dB beamwidth is about 95°. The return loss of the antenna is better than 15 dB.

In the second part of this thesis the bolometric power sensor integrated into DRW was designed, manufactured and tested at frequencies 75 – 1010 GHz. The power sensor consists of a metallic antenna -like structure in the center of the DRW in E-plane suspended on a membrane over an airgap to improve the thermal insulation. The power sensor showed good matching with the rectangular metal waveguides and constant responsivity over the wide band of frequencies, as well as a linear responsivity up to 500 mW applied power.

In the third part of this thesis the microelectromechanical system (MEMS) tunable HIS was developed for integration on to the surface of a DRW using suspended carbon nanotube (SWCNT) film as a movable element of the HIS. The implementation of a SWCNT network as a material for movable suspended film allows to significantly simplify the fabrication process of the HIS due to a simple technique of the SWCNT film deposition by dry transfer, and additionally it allows to reduce the actuation voltage of the HIS due to the low Young's modulus of the SWCNT network. The unique deposition technique of the SWCNT film allows to design a HIS phase shifter directly on the surface of the DRW. The suspended SWCNT film structure showed the tunability of the capacitance of 100% at 0 – 10 V applied bias voltage. Such properties allow to create a SWCNT MEMS HIS with a phase shift of 260° at 0 – 7 V bias voltage.

Keywords Dielectric rod waveguide (DRW), power sensor, bolometer, DRW antenna, THz, millimeter waves, MEMS, SWCNT, HIS

ISBN (printed) 978-952-60-6297-6 **ISBN (pdf)** 978-952-60-6298-3

ISSN-L 1799-4934 **ISSN (printed)** 1799-4934 **ISSN (pdf)** 1799-4942

Location of publisher Helsinki **Location of printing** Helsinki **Year** 2015

Pages 107 **urn** http://urn.fi/URN:ISBN:978-952-60-6298-3

Preface

This thesis work was carried out in the Department of Radio Science and Engineering of Aalto University School of Electrical Engineering between October 2010 and July 2015. I would like to thank my supervisor Professor Antti Räisänen for giving me the opportunity to work towards my doctoral degree, and for being always helpful and available, even during late evenings, weekends, and during vacation time.

I would like to thank my instructors: Dr. Dmitri Lioubtchenko for constant help, support, and ideas during all that time, and Juha Mallat for giving me valuable advices.

Big thanks to Dr. Victor Ovchinnikov for teaching me the basics of cleanroom microfabrication processes, helping to start my work in the cleanroom, and consultations through all the time of my thesis work. His help was very valuable during writing the articles included in this thesis.

Thanks to my colleague and co-author Dr. Ilya Anoshkin for bringing a completely new point of view to our work and for endless interesting ideas, as well as other co-authors for huge help in completing this work: Mr. Johannes Haimakainen, Prof. Albert Nasibulin, and Dr. Mikhail Erdmanis.

Thanks to the colleagues in the Department of Radio Science and Engineering: Mr. Vasilii Semkin, Ms. Irina Nefedova, Dr. Aleksi Tamminen, Dr. Aki Karttunen, Dr. Krista Dahlberg, Dr. Tero Kiuru, Mr. Subash Khanal, Dr. Juha Ala-Laurinaho, Dr. Risto Valkonen, Mr. Viktor Sibakov, Dr. Tomas Zvolensky, Dr. Dmitry Morits, Dr. Igor Nefedov, Prof. Sergey Tretyakov, Prof. Konstantin Simovski, Mr. Joni Vehmas, Mr. Kimmo Rasilainen, and many others. Special thanks to my friend and colleague Ms. Martta Olkkonen for great help during the doctoral studies.

In addition I would like to thank Prof. Vadim Atsarkin and Dr. Victor Demidov from the Kotel'nikov Institute of Radioengineering and Electronics of Russian Academy of Sciences, Moscow for guiding me during my master's thesis work, without them I wouldn't have decided to continue my studies towards doctoral degree. Thanks to Prof. Vladimir Lioubtchenko for introducing me to the topic of dielectric rod waveguides.

The research work described in this thesis has received funding from the Academy of Finland under the Centre of Excellence in Research Programme and DYMANITE project, GETA Graduate School in Electronics, Telecommunications and Automation, Aalto ELEC Doctoral School, and HPY Research Foundation.

Finally, thanks to my parents, Anatolii and Larisa, as well as my grandparents, Valerii, Galina, Jurii, and Tamara for huge support all the way through my studies no matter what. It is their effort which made me come so far.

And of course thanks to my brother Alexey for sharing all the good and bad moments with me and for motivating me all the time.

Espoo, 15 July 2015

Andrey Generalov

Contents

List of publications

This doctoral dissertation consists of a summary and of the following publications which are referred to in the text by their numerals

[I] A. A. Generalov, D. V. Lioubtchenko, and A. V. Räisänen, "Dielectric rod waveguide antenna for 220 – 325 GHz," in *Proc. of the 6th European Conference on Antennas and Propagation*, Prague, Czech Republic, 26-30 Mar. 2012, pp. 3551–3553.

[II] A. A. Generalov, D. V. Lioubtchenko, and A. V. Räisänen, "Dielectric rod waveguide antenna at 75 – 1100 GHz," in *Proc. of the 7th European Conference on Antennas and Propagation*, Gothenburg, Sweden, 8-12 Apr. 2013, pp. 541 – 544.

[III] A. A. Generalov, J. A. Haimakainen, D. V. Lioubtchenko, and A. V. Räisänen, "Wide band mm and sub-mm wave dielectric rod waveguide antenna," *IEEE Transactions on Terahertz Science and Technology*, vol. 4, no. 5, pp. 568–674, Sep. 2014.

[IV] A. A. Generalov, D. V. Lioubtchenko, J. A. Mallat, V. Ovchinnikov, and A. V. Räisänen, "Millimeter-wave power sensor based on silicon rod waveguide," *IEEE Transactions on Terahertz Science and Technology*, vol. 2, no. 6, pp. 623–628, Nov. 2012.

[V] A. A. Generalov, I. V. Anoshkin, M. Erdmanis, D. V. Lioubtchenko, V. Ovchinnikov, A. G. Nasibulin, and A. V. Räisänen, "Carbon nanotube network varactor," *Nanotechnology*, no. 26, 045201, Jan. 2015.

[VI] A. A. Generalov, D. V. Lioubtchenko, and A. V. Räisänen, "Reconfigurable mm-wave phase shifter based on high impedance surface with carbon nanotube membrane MEMS," *GSMM Global Symposium on Millimeter-Waves 2015*, Montreal, Canada, May 25-27, 2015.

Author's contribution

Publication [I]: "Dielectric rod waveguide antenna for 220 – 325 GHz"

The author performed the numerical simulations and the measurement campaign for the antenna. The author was responsible for writing the paper.

Publication [II]: "Dielectric rod waveguide antenna at 75 – 1100 GHz"

The author proposed the method of matching the single DRW antenna with different rectangular metal waveguides and investigated the performance of the antenna using numerical simulations. The author was responsible for writing the paper.

Publication [III]: "Wide band mm and sub-mm wave dielectric rod waveguide antenna"

The author estimated the optimal geometry of the antenna and compared the operation of the wide band and the narrow band DRW antennas, manufactured the antennas, assembled the experimental setup and analyzed the measurement data. The author was responsible for writing the paper.

Publication [IV]: "Millimeter-wave power sensor based on silicon rod waveguide"

The author performed the numerical simulations for the power sensor absorbance, performed the packaging of the power sensor and the measurement campaign, analyzed the results. The author was responsible for writing the paper.

Publication [V]: "Carbon nanotube network varactor"

The author was responsible for the design of the varactor, fabrication of the varactor support structure, performed the measurement campaign, analyzed the results and developed the SWCNT film deflection model. The author was responsible for writing the paper.

Publication [VI]: "Reconfigurable mm-wave phase shifter based on high impedance surface with carbon nanotube membrane MEMS"

The author was responsible for the development of the fabrication method of the SWCNT MEMS HIS and performing the numerical simulations of HIS operation. The author was responsible for writing the paper.

List of abbreviations

BWO	Backward wave oscillator
DRW	Dielectric rod waveguide
FIB	Focused ion beam
HFSS	High frequency structural simulator
HIS	High impedance surface
ICP-RIE	Inductively coupled plasma reactive-ion etching
MEMS	Microelectromechanical systems
NEP	Noise equivalent power
OEWG	Open ended waveguide
PECVD	Plasma enhanced chemical vapor deposition
PNA	Programmable network analyzer
PTFE	Polytetrafluoroethylene
RIE	Reactive-ion etching
SEM	Scanning electron microscope
SWCNT	Single-walled carbon nanotubes

List of symbols

A_C	Area of a parallel plane capacitor
A_{CS}	Area of a cross-section of the SWCNT film
C	Capacitance of the varactor
C_0	Capacitance of the varactor at zero bias voltage
C_{pp}	Parallel plane capacitance between meshes of slots
d	Width of the slots of the HIS
D	Period of the slots of the HIS
D_{ant}	The largest dimension of the antenna
E_x, E_y, E_z	x-, y-, and z- components of the electric field
E_Y	Young's modulus
F_C	Electric attraction force
F_E	Strain force
G	Thermal conductance
h	Thickness of the dielectric layer and the depth of the groove
h_2	Thickness of the second dielectric layer
h_{eff}	Mean distance between SWCNT film and metal contact
Δh	Maximum deflection of the SWCNT film
H_x, H_y, H_z	x-, y-, and z- components of the magnetic field
I	Bias current
j	Imaginary unit
k	Boltzmann constant
k_0	Wave number
k_{eff}	Effective wave number
k_x, k_y, k_z	x-, y-, and z- components of the wave number

L	Length of the groove
L_S	Series inductance
$M_{1..5}$	Amplitude coefficients
R	Resistance
R_V	Voltage responsivity of the power sensor
s	Width of the supporting dielectric
S_{11}	Reflection coefficient
t	Thickness of the SWCNT film
T	Temperature
V	Bias voltage
w	Width of the groove
w_0	Initial length of the SWCNT film suspended over the groove
$w(\Delta h)$	Length of a bended SWCNT film as a function of Δh
Z_h	Input impedance of the grounded dielectric layer
Z_S	Surface impedance of a grid of slots
Z_{S1}	Surface impedance of the first grid of slots
Z_{S2}	Surface impedance of the second grid of slots
Z_{tot}	Surface impedance of the HIS
$Z_{two-layer}$	Surface impedance of the two-layer HIS
α	Mesh parameter
β_1, β_2	Phase constants
γ	Additional coefficient
tan δ	Loss tangent
ε_0	Permittivity of free space
ε_D	Relative permittivity of dielectric
ε_{eff}	Relative effective permittivity
ε_r	Relative permittivity
ε_M	Relative permittivity of medium
η_{eff}	Effective wave impedance
η_M	Wave impedance of the medium

λ	Wavelength
μ_0	Permeability of free space
τ	Time
φ	Azimuth angle
ω	Angular frequency

1. Introduction

1.1 Background

The terahertz wave region is often defined as the frequency range between 0.3 – 3 THz of the electromagnetic spectrum [1, 2]. This part of the electromagnetic spectrum is also called as the submillimeter wave region. The millimeter wave region, on the other hand, is defined as a wave region corresponding to the wavelengths from 10 mm to 1 mm, which is in frequency range from 30 – 300 GHz. THz and mm-wave frequency systems are finding interest in high capacity communication systems [3], radars [4], imaging systems [5], material spectroscopy [6], medical diagnostics [7], biological studies [7, 8], radioastronomy [9] and other applications. This thesis work deals with the frequency range from 0.1 – 1 THz, which may be called as the sub-THz frequency range.

The terahertz wave radiation lies in the boundary region between lightwaves and microwaves. Both the radio-frequency technologies from one side of the spectrum and the optical technology from the other side are immature at the terahertz wave region [1].

1.1.1 Dielectric rod waveguides and antennas

A basic building block for all the radiowave systems is a waveguide and all the following devices are depending on the type of the waveguide. The most common transmission line in mm-wave technique is a hollow metal waveguide. With a growing frequency metal waveguides and other types of transmission lines possess high losses due to conduction loss in metal elements. Currently metal waveguides are available up to 1 THz, however their losses above 100 GHz are more than considerable.

A dielectric rod waveguide (DRW) is a rather novel type of waveguide which is especially advantageous in the sub-THz region due to smaller losses compared to any other waveguides [10, 11]. DRW can be made of a dielectric material with a dielectric permittivity higher than the permittivity of air, e.g. silicon, GaAs, or sapphire. In DRW the losses are determined only by dielectric losses, which are determined by a loss tangent, $\tan\delta$. For the non-doped high resistive semiconductors the loss tangent can be in the order of 10^{-4}. As a result, compared to standard rectangular metal waveguides, the DRW has lower losses, wider tolerance, and lower cost.

1.1.2 Microelectromechanical systems in mm-wave technology

Microelectromechanical systems (MEMS) have been developed in the last decades along the advances in microfabrication techniques and they have opened a new opportunity for various devices and sensors, such as accelerometers, temperature sensors, gas chromatographs and others. In the field of radio engineering, MEMS technology has allowed to create reconfigurable transmission lines, inductors, varactors, resonators and switches [12, 13]. In addition, carbon based materials, such as graphene and single-walled carbon nanotubes (SWCNT) attracted a great interest and offered a new opportunity for MEMS development due to unique mechanical and electrical properties of SWCNTs [14 - 16].

1.2 Objectives and scope of the thesis

The objective of this thesis work has been developing wideband DRW components at sub-THz frequencies, such as antennas, power sensors and phase shifters. The development of wide band DRW antennas [II, III] paves the way to integration of novel semiconductor THz sources directly on the DRW, which in combination with the DRW phase shifters [VI] and power sensors [IV] will result in complete THz system that can be used for diagnostics, spectroscopy or in other applications. The DRW THz technology will allow fabricating all the devices on the same substrate or waveguide, which will simplify the fabrication process, and could have advantage to other systems possessing lower losses.

The remaining of the thesis is organized in following manner:

Chapter 2 is devoted to the DRW antennas, numerical simulation, determining the optimal DRW antenna dimensions, and measurements of the antennas.

Chapter 3 is devoted to the DRW power sensor, numerical validation of the bolometer operation, demonstrating the operation of the power sensor and analyzing the results.

Chapter 4 is devoted to the SWCNT MEMS fabrication, extracting of the SWCNT film parameters, modeling the film deflection at applied bias voltage, designing the DRW HIS with a movable SWCNT membrane and estimating the phase shift of the resulting structure.

Chapter 5 gives summaries of publications, and Chapter 6 presents the conclusions and future work.

1.3 Scientific contribution

The scientific contribution of this thesis work can be explained with the following seven points:

1. Experimental verification of operation of DRW antenna at 220 – 325 GHz range. [I]
2. A method of matching a single DRW antenna with different rectangular metal waveguides was proposed and verified using numerical simulations. [II]

3. A manufacturing and measuring of a wide band DRW antenna for the frequency range of 75 – 325 GHz, the cross polarization levels of a DRW antenna were measured, the independence of radiation patterns on frequency was proven. [III]
4. A novel type of a DRW power sensor was experimentally demonstrated. [IV]
5. A novel fabrication method of the SWCNT suspended membrane was proposed and experimentally realized, the resulting structure is analyzed and allowed to extract parameters of the SWCNT film and model the film deflection. [V]
6. The high tunability of SWCNT MEMS varactor of 100% was achieved at 0 - 10 V bias voltage. [V]
7. The design of SWCNT MEMS HIS was proposed allowing to fabricate the HIS directly on the surface of the DRW and to achieve a 260° phase shift at 7 V bias voltage. [VI]

2. Dielectric rod waveguides and antennas

DRWs support propagating modes, and an infinite DRW with a constant cross section does not radiate [10, 17]. However, discontinuities in the DRW cause the propagating wave to radiate, hence the DRWs can be used as antennas [18]. The DRW antennas can be separated into two main groups by the type of radiation: end-fire antennas and leaky-wave antennas.

The leaky-wave DRW antennas have periodic discontinuities, which cause energy to leak from the antenna [19]. The angle of radiation from these antennas depends on frequency and they do not radiate to the boresight direction. The end-fire DRW antenna, on the other hand, radiates to the boresight direction and its radiation pattern is almost independent on frequency [20]. This thesis considers DRW end-fire antennas using rectangular metal waveguides for excitation [I - III].

2.1 Propagating modes in DRW

Two main types of DRW are used: with circular cross-section and with rectangular cross-section. The mode propagating in the DRW with a circular cross-section is HE_{11} mode [17]. The solution for the HE_{11} mode propagation in circular waveguides can be found analytically in terms of the Bessel functions, so circular DRWs are well studied. However, due to the problems and inconvenience of implementation of circular DRWs in, e.g., integrated circuits, this thesis is concentrating on the DRW with a rectangular cross section.

Modes in the rectangular DRW can not be calculated analytically, however there are approximate methods, such as Marcatili's [21] or Goell's [22] methods which allow to calculate the optimum cross-section of the rectangular DRW for the given material at the given frequency band.

Two sets of modes exist in a rectangular DRW: E^y_{mn} and E^x_{mn} [10, 17]. These modes are hybrid modes, in which indices x or y denote that the electric field is mainly polarized in these directions. Indices m and n denote the number of exterema of the field components in x and y directions, respectively. The desired mode in a rectangular DRW is a hybrid E^y_{11} mode (see Fig. 2.1).

According to Marcatili's approximation, E_y is the dominant electric field component of the E^y_{11} mode, and the other components are E_z, H_z, and H_x while E_x and H_y are negligible. The E_y and H_x field components of the E^y_{11} mode are cosinusoidally distributed inside the DRW and are decaying exponentially outside. The schematic field distribution for the E_y or H_x components

is shown in Fig. 2.1. The Marcatili's method considers only 5 regions for the calculation of the field distribution and propagation constant shown in Fig. 2.1. The shadowed regions are less essential for the waveguide properties and fields in these regions are not taken into account.

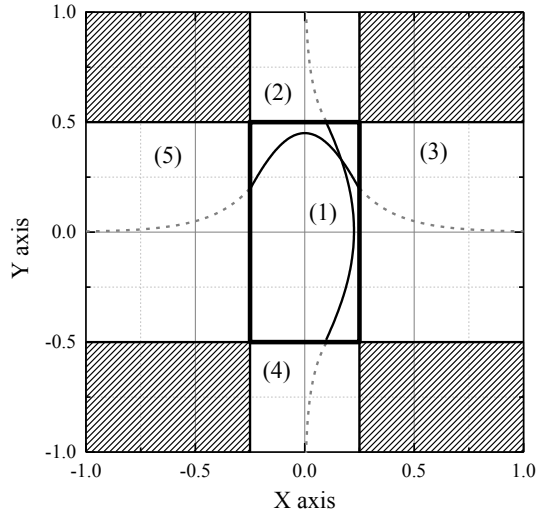

Figure 2.1. Schematic field distribution of E_y or H_x components of the propagating mode E_{11}^y in the DRW.

The H_x field component can be expressed as follows for the each of 5 regions (Fig. 2.1):

$$H_{x\nu} = \exp(-jk_z z + j\omega\tau)\begin{cases} M_1 \cos(k_x x + \beta_1)\cos(k_y y + \beta_2) & for \quad \nu = 1 \\ M_2 \cos(k_x x + \beta_1)\exp(-k_{y2} y) & for \quad \nu = 2 \\ M_3 \cos(k_y y + \beta_2)\exp(-k_{x3} x) & for \quad \nu = 3 \\ M_4 \cos(k_x x + \beta_1)\exp(k_{y4} y) & for \quad \nu = 4 \\ M_5 \cos(k_y y + \beta_2)\exp(-k_{x5} x) & for \quad \nu = 5 \end{cases} \qquad (2.1)$$

where $M_{1..5}$ are unknown amplitude coefficients, k_x and k_y are the propagation constants in region 1 (refractive index n_1) in the horizontal and vertical directions, respectively, k_{x3} and k_{y2} are the decay factors in the outer regions, and β_1 and β_2 are additional phase constants.

Marcatili's method allows to evaluate approximately the propagation constant for modes in a DRW with a given cross section and dielectric constant in a given frequency range. It is then possible to estimate the optimal cross section of the DRW for the single mode propagation regime in the given frequency range. The optimal cross-sections for a single E_{11}^y mode propagation in Si or GaAs DRWs are: 1.0 mm × 0.5 mm for 75 – 110 GHz range matched with WR-10 waveguide, 0.60 mm × 0.30 mm for 110 – 150 GHz range matched with WR-06 waveguide, and 0.30 mm × 0.15 mm for 220 – 325 GHz range matched with WR-03 waveguide [10, 11, 23].

2.2 Matching DRW with metal waveguides

The DRWs and DRW antennas are usually studied by exciting and matching the DRW with a rectangular metal waveguide [10, 20, 11] due to a wide availability of sources and devices based on rectangular metal waveguides, such as vector network analyzers. However the important advantage of the DRW is the possibility of integrating semiconductor devices into it. Hence DRWs will allow to develop future mm-wave and THz sources incorporated with DRW antennas [24, 25].

Previously DRWs and DRW antennas made of low permittivity materials, such as Teflon (ε_r = 2.1) or polyethylene (ε_r = 2.25), were studied [20]. Typically these DRWs have the same cross section as the rectangular metal waveguide, and thus additionally require structures such as a launching horn to decrease the losses in the transition. An example of such a launching horn is shown in Fig. 2.2 [20]. Launching horns may cause inconvenience of using such DRWs, and they increase the size and weight of the system.

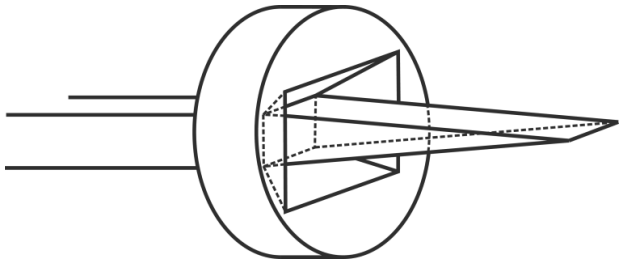

Figure 2.2. DRW antenna made of low permittivity material matched with a metal waveguide using a launching horn [20].

Using high permittivity materials, such as Si (ε_r = 11.68), sapphire (ε_r = 8.9 – 11.1), or GaAs (ε_r = 10.88) allows to match such a DRW with metal waveguides directly without using launching horns or other additional structures, which has been shown experimentally and by means or numerical simulations [10, 26-27]. In that case the cross section of DRW was smaller than the cross section of the metal rectangular waveguide for the same frequency band. The DRW of the smaller cross-section is inserted into the metal waveguide with a bigger cross section and the end of the DRW is tapered to reduce the insertion loss. The fundamental mode TE_{10} of the metal waveguide excites the E_{11}^{y} mode in the high-permittivity DRW [10], providing good matching and transmission. An example of a DRW antenna with a cross-section of 0.30 mm × 0.15 mm matched with WR-03 metal waveguide with cross-section of 0.43 mm × 0.86 mm is shown in Fig. 2.3.

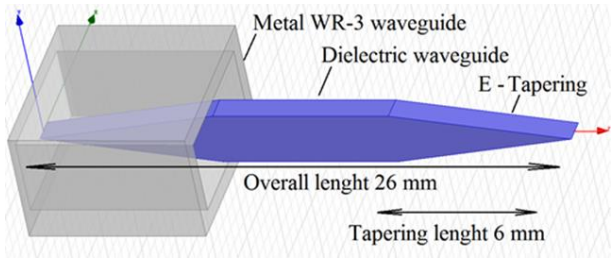

Figure 2.3. High permittivity DRW antenna matched with WR-03 waveguide.

Increasing the length of tapering allows to improve the matching of the DRW and metal waveguide. It was shown, e.g., for Si DRW of a cross section of 1.0 mm × 0.5 mm at 75 – 110 GHz that the reflection is reduced significantly as the tapering length increases up to 6 mm; above 6 mm the S_{11} is better than -20 dB [11]. These dimensions can be scaled for other DRWs with different cross-sections at different frequency ranges.

The single mode DRW antennas with different cross sections for each frequency range were studied, and they showed good performance: a DRW antenna with a cross-section of 1.0 mm × 0.5 mm for the 75 – 110 GHz range matched with the WR-10 waveguide, with a cross-section of 0.60 mm × 0.30 mm for the 110 – 150 GHz range matched with the WR-06 waveguide, and with a cross section of 0.30 mm × 0.15 mm for the 220 – 325 GHz range matched with the WR-03 waveguide [11]. One can note that the cross section of the antenna becomes smaller with increasing frequency, which results in fragility of the antenna and therefore in difficulties in manufacturing and operation. Another disadvantage of such an approach is the necessity to produce different rod antennas for every frequency range.

This thesis shows the possibility of using one DRW antenna over a wide frequency range. The antenna can be matched with different metal waveguides as it is schematically shown in Fig. 2.4. It is not necessary for the antenna to be fully inserted into the metal waveguide. It is enough if the tip of the antenna is inserted into a metal waveguide with a smaller size.

The cross-section of the antenna is 1.0 mm × 0.5 mm. Based on the observations stated above the length of the matching tapering is chosen to be 8 mm. Three different cases of matching the antenna with the WR-10, WR-05 and WR-03 waveguides are combined in Fig. 2.4.

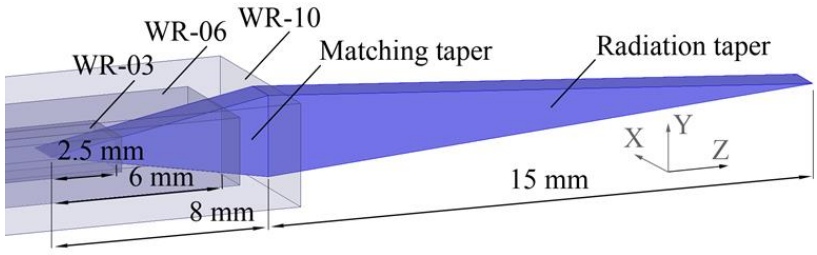

Figure 2.4. Geometry of the DRW antenna with alternative feed waveguides.

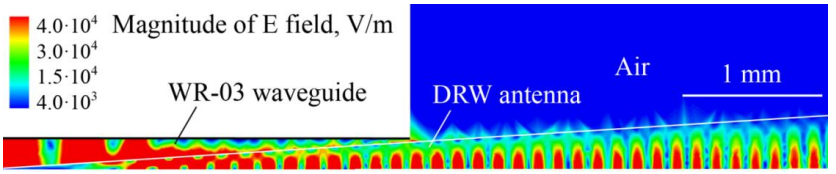

Figure 2.5. E field distribution in the transition from a WR-03 waveguide to a wideband DRW antenna.

The DRW antenna was simulated using Ansoft high frequency structural simulator (HFSS) software. The simulated electrical field distribution in the transition from metal WR-03 waveguide to a DRW antenna is shown in Fig. 2.5 at 300 GHz. The wave propagates from the metal waveguide to DRW and does not radiate further into the open space. Thus it shows that the DRW antenna can be matched with metal waveguides of different sizes.

The length of the insertion of the antenna into a metal waveguide can vary in the experiment due to the small sizes of the DRW antenna and metal waveguide and also due to mechanical backlashes of the experimental setup. Therefore the tolerance of the insertion length was studied. The comparison of S_{11} for antenna with different insertion length into the WR-03 waveguide is shown in Fig. 2.6. One can see that the matching improves as the antenna is further inserted into a waveguide. An improvement is noticeable until the insertion length of 1.5 mm for the WR-03 band, and for the lengths of 1.5 – 2.5 mm it does not change noticeably; S_{11} is better than -25 dB.

S_{11} of the DRW antenna with the same geometry and the cross section of 0.3 mm × 0.15 mm designed for matching with the WR-03 waveguide is shown in Fig 2.6 for comparison. One can see that S_{11} of the antenna with the cross section of 1.0 mm × 0.5 mm is not worse than that of the antenna with the cross section of 0.3 mm × 0.15 mm, hence there are no drawbacks of using the antenna with a bigger cross section in terms of matching.

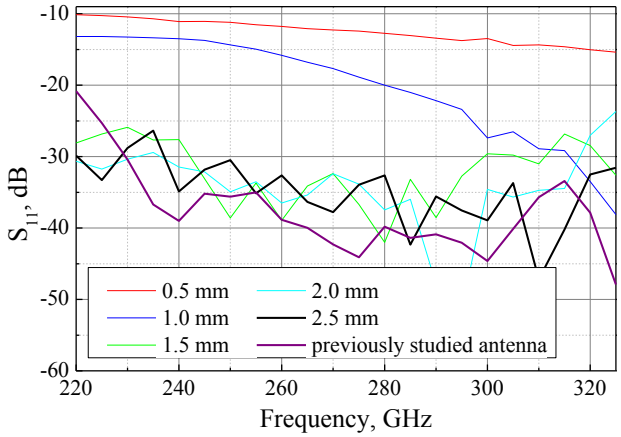

Figure 2.6. S_{11} of the wideband DWR antenna at different insertion length into WR-03 waveguide and S_{11} of a single mode DRW antenna fully inserted into WR-03 waveguide.

The widths of WR-2, WR-1.5 and WR-1 waveguides are smaller than that of the DRW antenna (0.5 mm); hence the DRW antenna can not be inserted into those waveguides. The transition that was used to simulate the matching of the DRW antenna with those waveguides is shown in Fig. 2.7. The size of the waveguide for impedance matching of the antenna must be the same in the E plane and the tapering of the transition is done only in the H plane. The angle of tapering is chosen to be 10°.

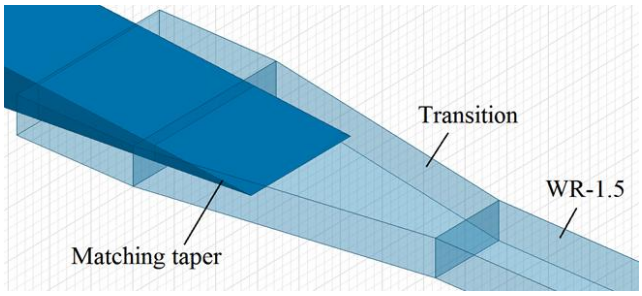

Figure 2.7. The transition between WR-1.5 waveguide and DRW antenna.

The simulated S_{11} parameters are presented in Fig. 2.8 for waveguides from 75 to 1100 GHz. It is shown that the matching is good for the whole frequency range and S_{11} is better than -20 dB. For the WR-2, WR-1.5 and WR-1 bands the simulation is carried out with the transition shown in Fig. 2.7. One can see in Fig. 2.8 that the transitions provide a good matching of the DRW antenna with the metal waveguides.

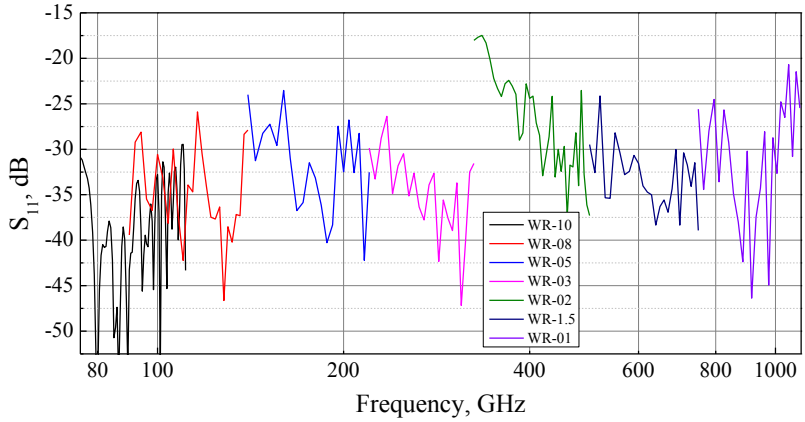

Figure 2.8. Simulated S_{11} of the DRW antenna matched with different waveguides.

2.3 Antenna tapering and radiation pattern

The radiation tapering of the antenna defines its radiation pattern. The tapering can have either a linear or non-linear profile. Non-linear profile DRW antennas were studied by several authors [28, 29] and an improvement of gain of the antennas was achieved. However, there are two main problems with

non-linear tapers: first, it is very difficult to produce non-linear tapers for high permittivity mm-wave DRW antennas made of Si, GaAs, or sapphire, and second, the non-linear profile compromises the wideband performance of the antenna. Hence, the antennas described in this thesis have linear profile tapering.

Linear tapers of the DRW antenna can be of three types: E-plane (YZ in Fig. 2.4), H-plane (XZ in Fig. 2.4) or pyramidal tapers. It was shown in [20] that the E-plane tapers and pyramidal tapers provide the same performance of the antenna in terms of beamwidth and gain, while the H-plane taper performs significantly worse. Since it is technologically difficult to produce pyramidal tapers, both ends of the antenna are chosen to be E-plane tapered.

The radiation from an E-plane taper of a single mode DRW antenna with the cross-section of 0.30 mm × 0.15 mm at 300 GHz is illustrated in Fig. 2.9. In that case the wave propagates in the single mode E_{11}^{y} regime and radiates into free space as the cross section becomes narrower at the taper.

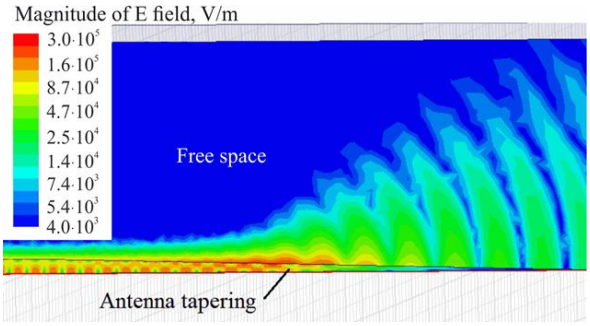

Figure 2.9. Simulated E field distribution in the vicinity of the tapering of the single mode DRW antenna.

In contrast, the proposed wideband DRW antenna has a bigger cross-section; but that does not affect the radiation or matching, which will be illustrated further. The radiation from the wideband DRW antenna at 300 GHz is illustrated in Fig. 2.10. The wave propagates in a single mode regime in the transition from the metal waveguide to the DRW antenna (Fig. 2.5) and to the beginning of the radiation tapering (Fig. 2.10). The comparison between two antennas matched with the WR-03 waveguide is shown in Fig. 2.11.

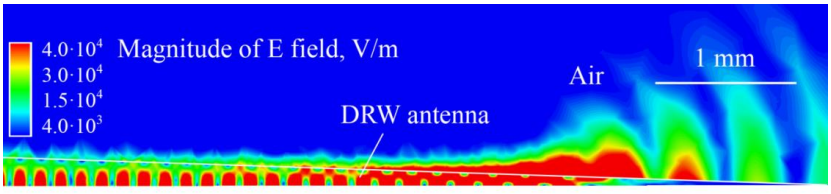

Figure 2.10. Simulated E field distribution in the vicinity of the tapering of the wideband DRW antenna.

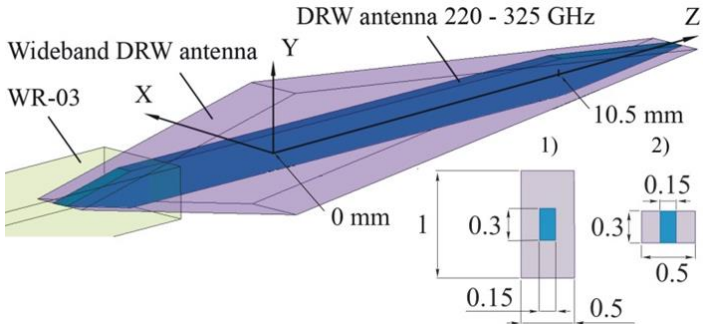

Figure 2.11. Comparison of the dimensions of the wideband antenna and the single mode DRW antenna. 1) – cross section at Z = 0 mm, 2) – cross section at Z = 10.5 mm. Dimensions are in millimeters.

Fig. 2.12 shows the comparison of simulated field distributions inside the DRW for the case of the antenna under study with the maximum cross section of 1.0 mm × 0.5 mm and for the optimized antenna with a cross section of 0.3 mm × 0.15 mm (Fig. 2.11) which is designed to operate in the single mode regime. It can be seen, that at Z = 0 (maximum cross section) the electric field distribution is wider for the antenna under study, however it has only one maximum in both X and Y directions. Moving along the tapering the field becomes more concentrated in the rod, and at Z = 10.5 mm, when the Y dimension of the two antennas coincides, the field distribution in the Y direction is almost the same for both antennas. The X dimension of the antenna under study is constant, thus the shape of the field distribution in the X direction does not change along the rod and it is wider than the field distribution for the antenna with a smaller cross section.

Furthermore, the comparison of radiation patterns for the two antennas is shown in Fig. 2.13, and it can be seen that the radiation patterns are identical. It shows that one antenna with a larger cross section can be used in a wide range of frequencies and it operates the same way as the antennas designed and optimized for the single mode regime at a given frequency.

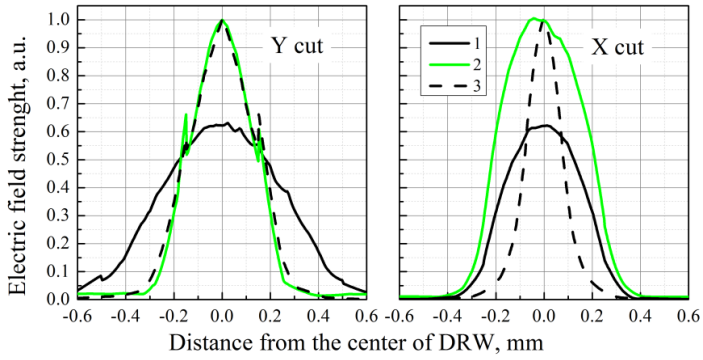

Figure 2.12. Comparison of the simulated electric field distributions inside of DRW antennas at 300 GHz: 1 – field distribution for the wideband antenna at Z = 0 mm (1.0 mm × 0.5 mm); 2 – field distribution for the wideband antenna at Z = 10.5 mm (0.3 mm × 0.5 mm); 3 – field distribution for the single mode antenna at Z = 10.5 mm (0.3 mm × 0.15 mm). See Fig. 2.11.

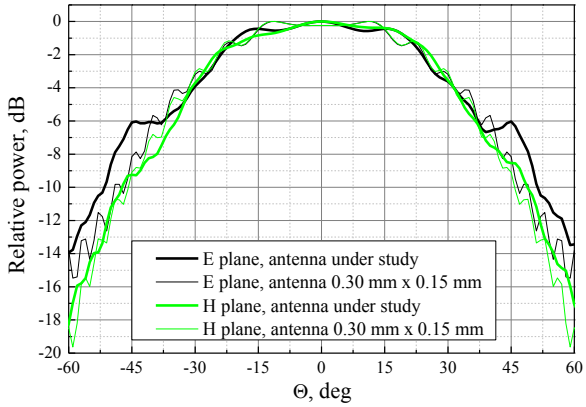

Figure 2.13. Comparison of the simulated radiation patterns of two antennas: wideband DRW antenna and single mode DRW antenna with the cross section of 0.30 mm × 0.15 mm in E and H planes at 300 GHz. See Fig. 2.11.

The effect of radiation tapering length on the radiation pattern of the DRW antenna is shown in Fig. 2.14. The simulations are performed for the antenna with a matching tapering length of 8 mm. The radiation patterns are presented for radiation tapering lengths of 10, 12, 15 and 20 mm at 300 GHz in the E plane. It is shown, that as the radiation tapering length increases, the radiation pattern becomes narrower and the side lobes become smaller, which agrees with previous observations for the single mode DRW antennas [20, 30]. However, it is difficult to manufacture the antennas with long tapering since the tip becomes fragile. Therefore, 15 mm seems to be the optimal tapering length.

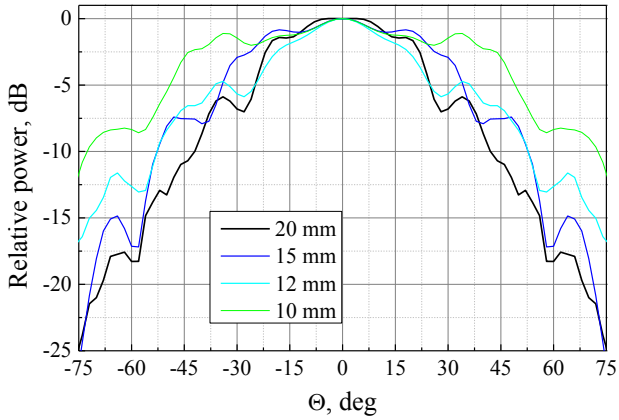

Figure 2.14. Radiation patterns of the antennas with different radiation tapering lengths at 300 GHz.

The desirable polarization of the antenna is along the Y direction (Fig. 2.11). Hence the magnitude of the cross polarized component of the field must be studied. Simulated cross-polarization (X component) radiation patterns are shown in Fig. 2.15 for frequencies 85 GHz (top) and 280 GHz (bottom). The

amplitudes are normalized to maximum amplitudes in co-polarization at boresight direction.

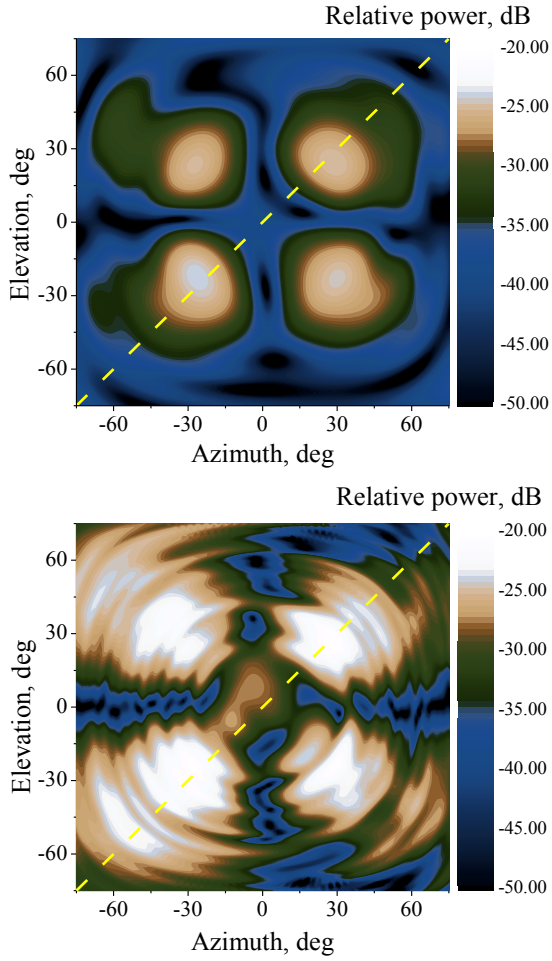

Figure 2.15. Simulated cross-polarization radiation patterns of the antenna at 85 GHz (top) and 280 GHz (bottom). Dashed lines indicate cross-sections at $\varphi = 45^{\circ}$. The slight asymmetry is due to numerical errors caused by asymmetric mesh in HFSS simulation.

2.4 Antenna fabrication and measurement setup

The tapered DRW antenna was manufactured using a dicing saw with a diamond blade of 20 µm thickness. It was cut from a double side polished high-resistivity GaAs wafer of 500 µm thickness. The dimensions of the antenna in the H-plane are defined by the wafer thickness and the geometry of the antenna in the E-plane is defined by the cuts of the saw. Finally the antenna was cut with a cross section of 1.0 mm × 0.5 mm with tapers of 8 mm and 15 mm long. A photograph and a microscope close-up image of the fabricated antenna are shown in Fig. 2.16.

After cutting, the antenna was mounted in a Styrofoam holder and this holder was attached to a positioning stage, which allows the accurate insertion of the DRW antenna into the metal waveguide.

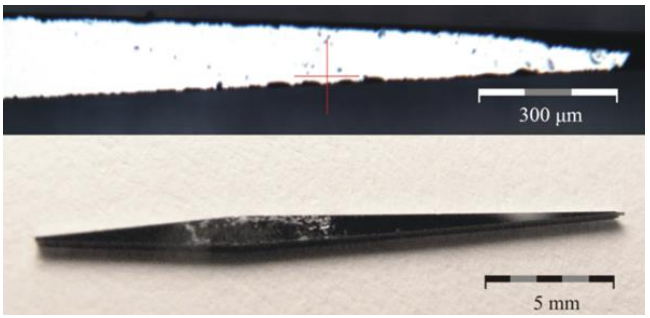

Figure 2.16. A microscope image (top) and a photograph (bottom) of the fabricated DRW antenna.

S-parameters of the antenna were measured with Agilent E8361C PNA using WR-10, WR-06, WR-05 and WR-03 waveguide extensions. In case of the WR-10 waveguide the antenna was inserted to the waveguide at full length of the matching taper, i.e. 8 mm (see Fig. 2.4), and in case of the WR-06, WR-05, and WR-03 waveguides the antenna was inserted up to the maximum possible length, 6.0 mm, 5.5 mm, and 3.5 mm, respectively.

The radiation patterns at different frequencies were measured using an ABmm vector network analyzer and a planar scanner. The measurements were done in the far field since for the end-fire DRW antenna the far-field distance is small. According to the generally used criterion, the far-field distance equals to $2D_{ant}^2/\lambda$, where D_{ant} is the largest dimension of the antenna, and λ is a wavelength. The largest dimension of the antenna is 15 mm in Z direction (Fig. 2.4). However, for the end-fire antenna the dimensions of the cross-section are more important, and the higher is the frequency, the smaller part of the tip behaves as a radiator. As it was shown in [31], the phase center of the DRW antenna moves closer to the tip as the frequency increases, which results in a smaller effective aperture size of the DRW antenna. Results shown in Fig. 2.10 agree well with the above mentioned observation: the effective size of the antenna in the Z direction is of the order of 3 – 4 mm at 300 GHz, and the cross section is less than 0.3 mm × 0.5 mm (Fig. 2.11). This results in the far-field distance by any criterion of only 30 mm or less. The measurements were performed at a distance of 100 mm.

The experimental setup for measuring the radiation patterns is shown in Fig. 2.17. The antenna was glued to a holder and attached to a 6-degrees-of-freedom positioning stage. The ABmm vector network analyzer was used in 3 frequency bands: 75 – 110 GHz with the WR-10 waveguide, 110 – 170 GHz with the WR-06 waveguide and 220 – 325 GHz with the WR-03 waveguide. The antenna was aligned and inserted into a metal waveguide using a positioning stage. An open ended waveguide (OEWG) probe was used to sample the far field.

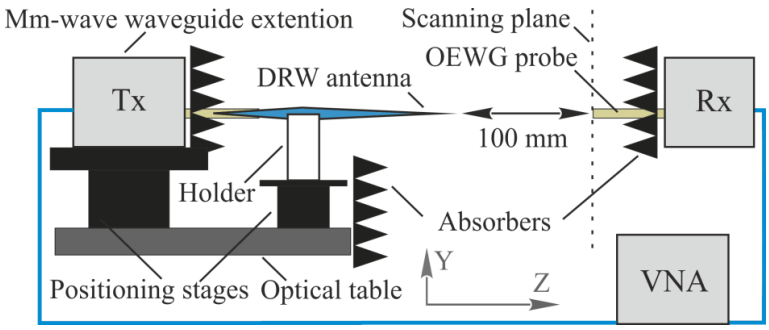

Figure 2.17. Experimental setup for measuring the radiation patterns.

2.5 Measurements and results

The measurement results together with the simulated results for the antenna matching are shown in Fig. 2.18. One can see that the measurement data correspond well with simulated results at 75 – 110 GHz (WR-10), 110 – 170 GHz (WR-06), and 140 – 220 GHz (WR-05). However, at 220 – 325 GHz (WR-03) the measured reflection is higher than the simulated one. It can be explained by the fact, that the tip of the antenna is not perfect.

One can see in Fig. 2.16 that the tip of the antenna is broken and the cracks on the surface have dimensions of the order of 100 μm. At lower frequencies when the cracks are much smaller than the wavelength, the unideality does not affect the results. At 300 GHz the wavelength is 1 mm in free space and inside the DRW it is of the order of 300 μm, so the cracks of the antenna are of the order of quarter of a wavelength. As it can be seen in Fig. 2.18, it results in smaller return loss than that expected from the simulation results. At frequencies higher than 300 GHz the cracks affect results much more and it is not possible to use this antenna. Therefore, due to current manufacturing equipment in our laboratory the operational frequency of the antenna is limited to 325 GHz (WR-03 waveguide band). However, using a modern and more advanced dicing saw it will be possible to fabricate an antenna with smoother surface and increase the highest operational frequency.

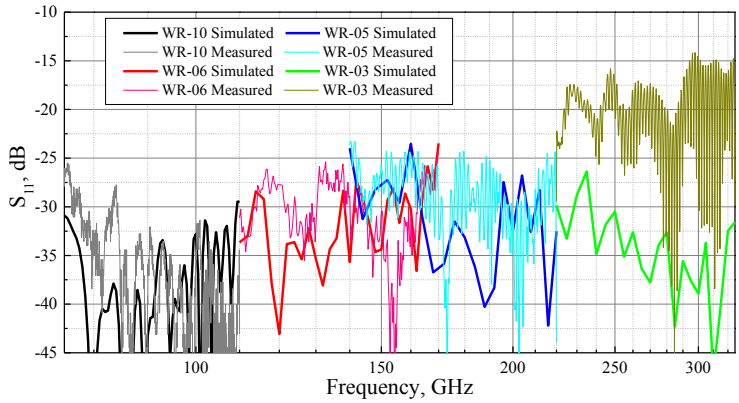

Figure 2.18. Measured and simulated S_{11} parameter of the antenna.

The measurement results for the vertical (E-plane) and horizontal (H-plane) cuts of the radiation patterns are shown in Figs. 2.19 and 2.20 together with the simulation data. The measurement data were transformed from planar coordinates to spherical coordinates and a probe correction for the open ended waveguide was added. Instead of using an open-ended waveguide (OEWG) probe correction presented in [32], we used a simulated (HFSS) radiation pattern for the probes at different mm-wave bands. The simulated radiation patterns of the OEWG probes differ from the calculated radiation patterns of [32] by a factor of 1.5 for the E plane radiation pattern and factor of 0.75 for the H plane radiation pattern. The measurement results in Figs. 2.19 and 2.20 correspond well with the simulation results, however at frequency 280 GHz the discrepancy between the measured and simulated data is more considerable. It can be explained by the quality of the tip of the antenna and asymmetry. The beamwidths of the antenna at different frequencies are presented together in Table 2.1.

The gain of the antenna was measured using a three antenna method [30] at 95 GHz, 120 GHz, and 160 GHz. The measured gain of the antenna is 9.8 dB, 10.8 dB, and 10.3 dB, respectively. The uncertainty of the measurements was about 0.3 dB and it is caused by uncertainty of the gain of the reference antennas and uncertainty of the distance between the antennas. For comparison it is possible to estimate the gain of the antenna knowing the very low losses of the DRW and using the 3 dB beamwidth values given in Table 2.1. According to Table 2.1 the gain is about 10 dB over the whole frequency range measured.

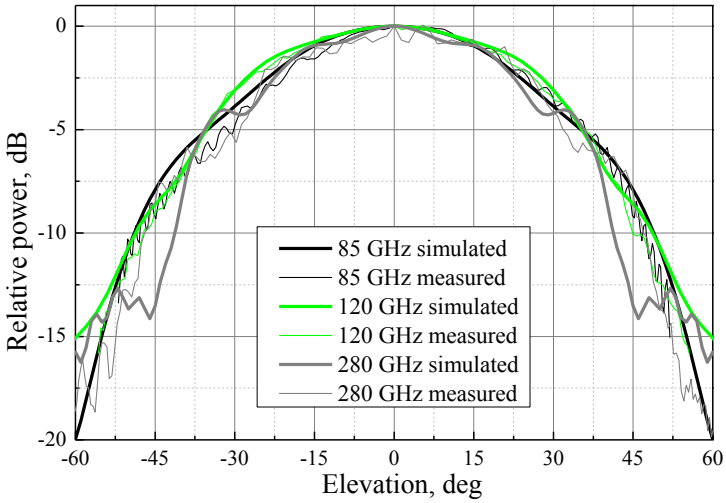

Figure 2.19. Measured and simulated E plane radiation patterns of a wideband antenna at different frequencies.

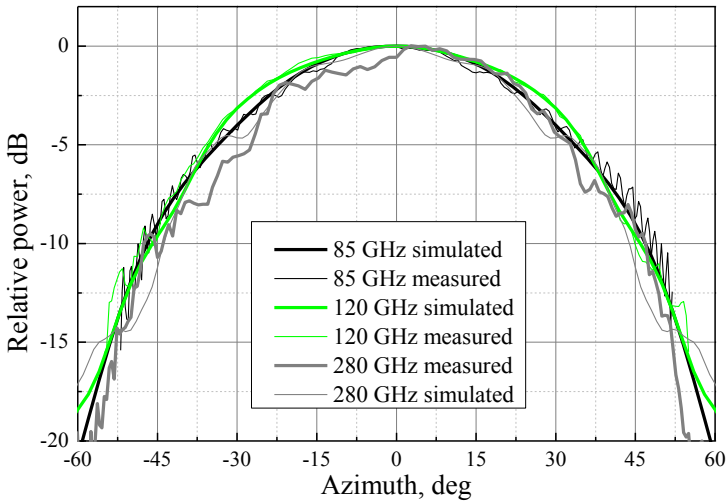

Figure 2.20. Measured and simulated H plane radiation patterns of a wideband antenna at different frequencies.

Table 2.1. Antenna beamwidths at different frequencies (in degrees).

Frequency, GHz	E plane				H plane			
	3 dB		10 dB		3 dB		10 dB	
	meas.	sim.	meas.	sim.	meas.	sim.	meas.	sim.
85	51	52	96	98	52	52	96	94
95	57	56	92	95	59	56	96	94
120	51	48	95	94	60	60	91	92
140	51	48	94	83	58	54	92	92
160	56	50	98	94	52	54	84	89
280	58	54	94	94	49	48	91	88
310	57	58	92	98	58	66	94	94

The radiation patterns of the antenna in cross-polarization were measured using the same setup shown in Fig. 2.17 but turning the OEWG probe 90 degrees using a waveguide twist, so the X component of the field was measured. The measurement results of cross-polarization are presented in Fig. 2.21 together with the simulated results. Since the radiation patterns of the antenna consist of 4 lobes, the results are presented as cross-sections at $\varphi = 45°$ (See Fig. 2.15) in contrast with results of co-polarization measurement, which are presented in the E-plane at $\varphi = 90°$ and in the H-plane at $\varphi = 0°$.

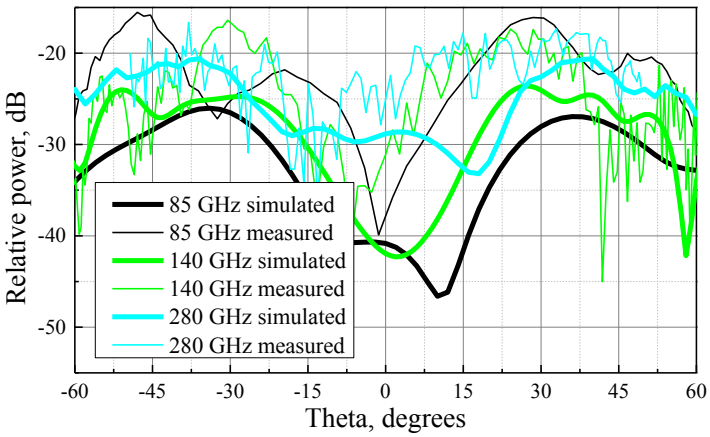

Figure 2.21. Simulated and measured cross-polarization radiation patterns of the antenna. Presented are cross-sections at $\varphi = 45^{\circ}$ (see Fig. 2.15).

3. DRW power sensor

The power sensor is intended to measure the power of incident radiation or power of the travelling wave in a waveguide. There are numerous power sensors available for microwave, mm-wave, THz and infrared range [33], usually they are integrated with an antenna [34 - 36], integrated into a metal waveguide [37], or using a fin-line [38]. However, the DRW requires a new approach to integrate the power sensor into it. In this chapter the DRW power sensor is studied and tested as a terminating load in the metal waveguide [IV], which is common in power meter applications. As a result, the power sensor can measure the power of mm-waves travelling in the DRW. Subsequently, it can be used in devices based on DRW such as controllable DRW antennas [III], as well as antenna arrays [39].

3.1 Bolometer power sensors

Bolometer power sensors play a significant role in power measurements. A direct detection bolometer power sensor detects the heating caused by absorption of RF, millimeter wave, or infrared power [33, 40]. The absorbing element is usually realized in a form of thin membrane to reduce the thermal capacity and thermal conduction [40 - 42]. The heating in direct detection bolometers causes the change in the resistance of the absorbing element, which is next measured. However, the temperature change can be also measured using thermocouples [43], electron heating effect in *n*-Si [37], or temperature-dependent kinetic inductance [44].

The most sensitive bolometer sensors ate the superconducting bolometer sensors, which utilize the steep resistance-temperature dependence of superconductors near the critical temperature [45]. Superconducting bolometer sensors are used in the most sensitive mm-wave and THz measurements, mostly in radio astronomy [45] and mm-wave imaging [35] or security applications [46]. For the spectroscopy and radio astronomy applications the heterodyne mixer detectors are needed, which additionally require THz local oscillator source [47, 48].

While superconductor bolometers and bolometer mixers offer outstanding sensitivity and widely used in radioastronomy, the resulting detection systems are complicated due to the need of cryogenic cooling of THz local oscillators, hence the is still a need for a cheap room-temperature bolometers. This chapter presents a thin metallic room temperature bolometer structure integrated into DRW [IV].

3.2 Design of a DRW power sensor

The power sensor consists of a metallic structure which absorbs mm-wave power and is therefore heated, causing a change of its resistivity. The structure is integrated into a center of a DRW parallel to the E plane so that it absorbs the energy of the wave propagating in the DRW. The schematic view of the metallic structure integrated into the DRW is presented in Fig. 3.1. The shape of the bolometer comes from the need to produce a gradually absorbing structure that has dimensions comparable to a wavelength. The shape of the metallic bolometer structure was studied using Ansoft HFSS software. Fig. 3.2 shows the volume loss density in the transition between a WR-10 metal waveguide and the DRW with the integrated bolometer structure. The simulations results show that the bolometer provides the best matching if the square resistance of the metal film is about 20 Ω/sq. The bolometer is a long stripe of metal and it consists of about 100 squares resulting in an overall resistance of about 2 kΩ.

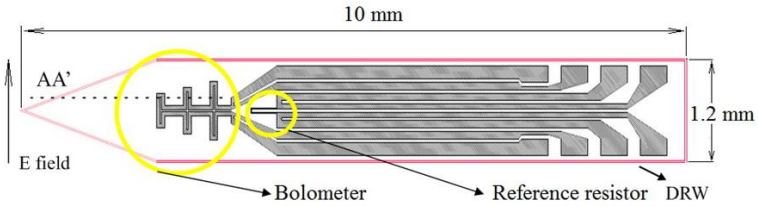

Figure 3.1. A design of the power sensor.

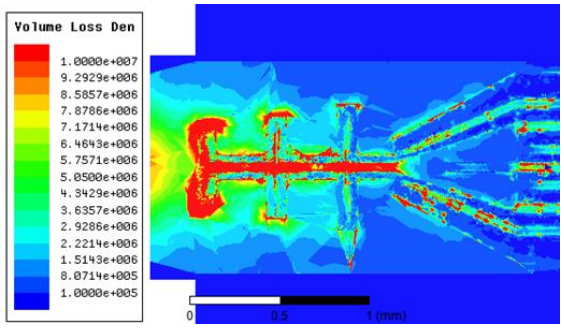

Figure 3.2. Volume loss density in the transition between the metal waveguide and DRW with the integrated bolometer structure at 90 GHz.

The metallic structure consists of the bolometer and a reference resistor (Fig. 3.1). The bolometer absorbs the power and it is thermo-insulated from the DRW, while the reference resistor is a small stripe of metal which is in thermal contact with the DRW and is considered not to absorb the incident millimeter wave power. Thereby, the reference resistor can detect the heating caused by the changes in the environment not related to the absorption in the bolometric structure, which allows to subtract the errors caused by the instability of the environment, e.g. temperature changes. As one can see in Fig. 3.2, the volume

loss density is higher around the bolometer structure than that around the reference resistor, which indicates that the resistor absorbs a negligible part of power compared to the bolometer structure. The presence or absence of the reference resistor does not influence to the simulation results. The reference resistor is a stripe of metal which consists of the same amount of squares as the bolometer structure. The scheme is designed for 4 wire measurements of the reference resistor and the bolometer to improve the precision of the measurement.

The width of the prototype of the power sensor layout is less than 1.2 mm; it is integrated into a DRW with the cross section of 0.6 mm × 1.2 mm, which allows to insert and match the DRW with the power sensor into a WR-10 waveguide with the size of 1.27 mm × 2.54 mm. The size of the structure is limited only by a lithography resolution; therefore the power sensor can be scaled down and integrated into DRWs of different sizes.

3.3 Thermal insulation of the bolometer

To achieve higher sensitivity and diminish the influence of a substrate temperature on the bolometer, it must be thermally insulated. The insulation can be done by suspending the bolometer on a membrane above an airgap.

To estimate the efficiency of thermal isolation of a bolometer suspended on a membrane, simulations have been performed for two bolometer designs: a bolometer suspended on a SiO_2 membrane, and a bolometer deposited on a polymer film (PTFE). The simulations have been performed in COMSOL Multiphysics 3.5a. In both simulations it is supposed that mm-wave power of 0.1 mW is dissipated in the metal element. The temperature distributions for both variants are shown in Fig. 3.3 in color scale. The cooling only by thermal conductivity from the metallic bolometer structure to the Si DRW through the membrane or the PTFE substrate is taken into account. The maximum temperature increase of the bolometer structure vs. heating time is shown in Fig. 3.4. One can see in Fig. 3.4 that the maximum overheat of the PTFE film and the air-gap-isolated metallic bolometer structure is 0.05 °C and 0.35 °C, respectively. Additionally, the bolometer on a PTFE film is slower. The temperature is saturated after 0.07 s in the bolometer on a PTFE film, in comparison with 0.03 s in the case of the cantilever one.

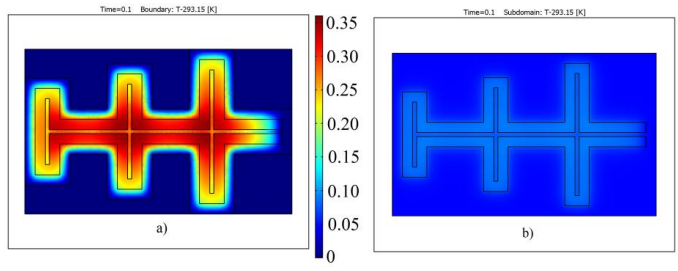

Figure 3.3. Overheat temperature distributions of the bolometers at DC with different thermal isolation: a) 50 μm air gap and 1 μm thick SiO_2 cantilever (undercut is 50 μm); b) 50 μm PTFE layer.

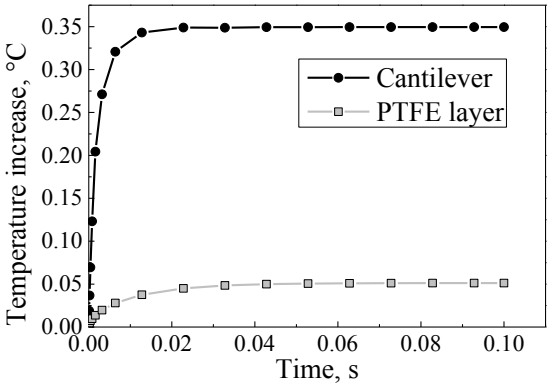

Figure 3.4. Transient curves of the temperature in the hottest points of the bolometer on cantilever and on PTFE film.

The optimal values of the gap and lateral undercut for the cantilever sensor are found on the base of simulations and show that increasing both parameters improves the sensor functionality. At the same time, technologically acceptable value for the undercut is about 50 μm and it already provides reasonable overheat. That is why experimental samples were fabricated with a gap and undercut of 50 μm. The airgap will affect the performance of the device only if the size of an airgap is comparable to the wavelength, hence the 50 μm airgap can be used at frequencies up to approximately 1 THz (300 μm wavelength).

3.4 Fabrication

The fabrication of the power sensor is done using Si dry etch on a high-resistivity Si substrate. The thermo-insulation of the bolometer structure is provided by a SiO_2 membrane. The fabrication steps are shown in Fig. 3.5. First, the Cr metallic structure of the thickness of 100 nm is deposited and patterned on top of SiO_2 layer (a). Next, the structure is covered by a layer of Al_2O_3 (b), (c), which will protect the structure during Si and SiO_2 etching. Then the SiO_2 layer is etched between the metallic structure (d) and after that the Si substrate is etched using inductively coupled plasma reactive-ion etching (ICP-RIE) (e) with the undercut which provides the thermo-insulation. Thereby the metallic bolometer structure is suspended in the air by a 50 μm SiO_2 membrane. The membrane is fixed to the Si DRW only by one edge. This design significantly simplifies the fabrication process of the sensor.

In Fig. 3.6 scanning electron microscope (SEM) images of the SiO_2 cantilever cut at AA' plane (see Fig. 3.1) are shown. The cross section corresponds to the schematic in Fig. 3.5 e). After 40 minutes etching in ICP-RIE the gap depth and lateral undercut reach 80 μm and 60 μm, respectively. The lighter color between gaps shows the long channel along the symmetry axis of the structure.

Finally, the DRW consist of two halves: the sensor chip with a metallic structure and a cover chip. After the fabrication they are bonded together using SU-8 photoresist so that the metallic structure is located in the center of the DRW.

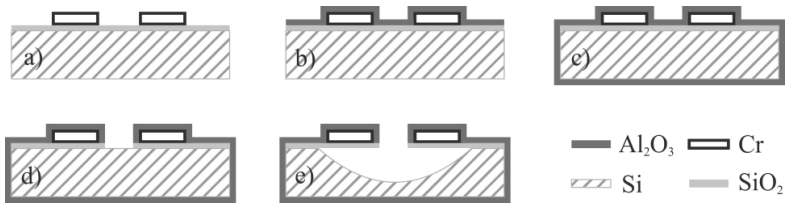

Figure 3.5. Fabrication steps of the power sensor.

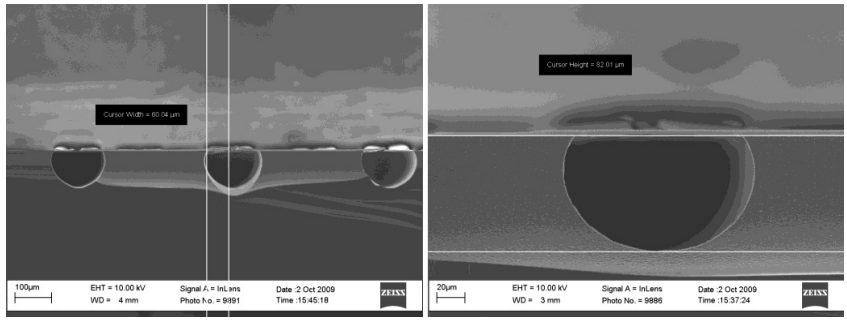

Figure 3.6. SEM images of 1 µm thick SiO_2 cantilever cut at AA' plane (see Fig. 3.1) with different magnifications. a) three arms of metallic structure with etched gaps (lateral undercut is 60 µm); b) central arm (depth of etching is 82 µm).

3.5 Measurements and results

A schematic overview of the experimental setup is shown in Fig. 3.7. Several power sources were used to generate power at different frequencies: Gunn oscillators were used at 45 – 150 GHz with output power up to 25 mW, backward wave oscillators (BWO) at 640 – 1000 GHz with output power up to 10 mW and a magnetron at 94 GHz with average output power up to 500 mW. The transition to the WR-10 waveguide was used if needed and the power sensor was inserted into an open end of the waveguide. In the case of measurements at 45 GHz the power sensor was inserted into the center of a WR-19 waveguide. A photograph of the power sensor prototype ready to be inserted into a WR-10 waveguide is shown in Fig. 3.8. In the case of Gunn oscillators, the power sources were set to generate maximum possible power and the output power was varied by an attenuator. For the frequencies above 150 GHz the power source was BWO. Three BWOs were used to generate power at frequencies of 640, 820, and 1010 GHz. The power was varied by changing the cathode current of the BWO. The output power of the source was first measured by a Dorado DPM-2A colorimeter power meter. The resistance change of the power sensor was measured with an HP 3478A multimeter using a 4 wire method.

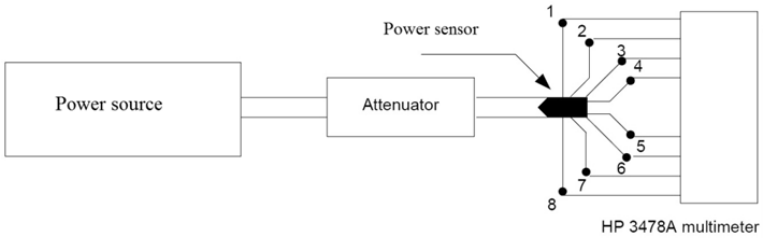

Figure 3.7. Experimental setup scheme.

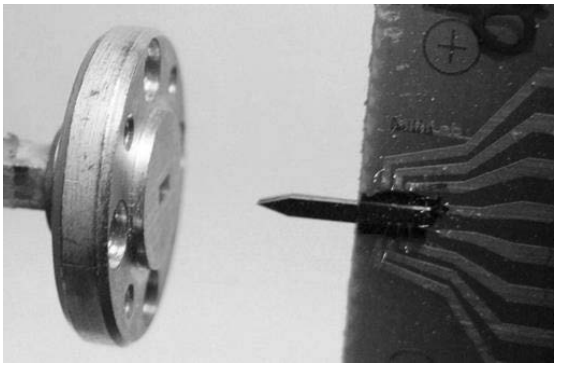

Figure 3.8. A photograph of the power sensor ready to be inserted into a WR-10 waveguide. The sensor is glued and contacts of the sensor are bonded to a printed circuit board.

The matching of the devices with a WR-10 waveguide was measured at W band, shown in Fig. 3.9 together with the simulations results. One can see that S_{11} is less than -17 dB over the whole band. Simulations show also that S_{12} is below -25 dB which means that the bolometer structure absorbs about 98% of incident power.

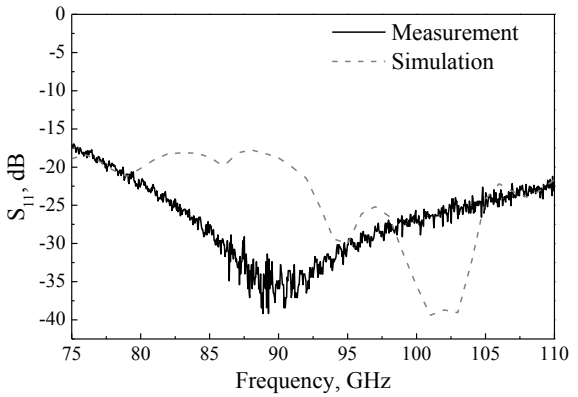

Figure 3.9. Measured and simulated S_{11} parameter for the power sensor at W band.

Power measurement results are shown in Figs. 3.10 – 3.12. The value plotted on the graphs is $\Delta R = R - R_0$, where R is the resistance at applied power, R_0 is the resistance at $P = 0$. The value of R_0 for the sensor under test is 1.81 kΩ. Resistance change measurements are carried out automatically with HP 3478A

multimeter. The amount of bias current generated with the HP3478A multimeter is I = 1 mA, which gives the bolometer constant DC heating and does not affect measurements of mm-wave heating. One can see in Figs. 3.10 – 3.12, that the resistance of the bolometer changes linearly on the power.

Fig. 3.13 shows the dependence of the slope $\Delta R/\Delta P$ versus frequency. The uncertainty of the values at frequencies lower than 150 GHz is about 1 dB. The uncertainty of the BWO measurements at higher frequencies (Fig. 3.11) is higher due to uncertainty of the output power of the BWO. The dashed line in Fig. 3.13 shows the average slope, which is 0.51 Ω/mW.

The power sensor was also tested with DC power applied up to 200 mW and showed no signs of burnout or degradation, which can be considered as a good tolerance to high power.

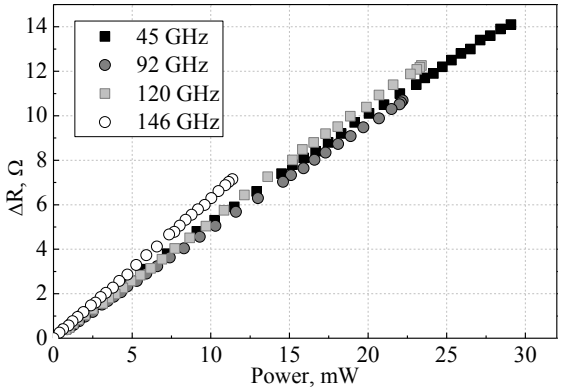

Figure 3.10. Results of measurements for the sensor prototype using Gunn oscillators power sources.

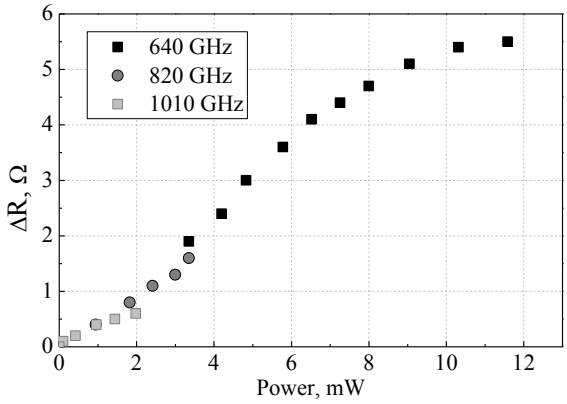

Figure 3.11. Results of measurements for the sensor prototype using BWO power sources.

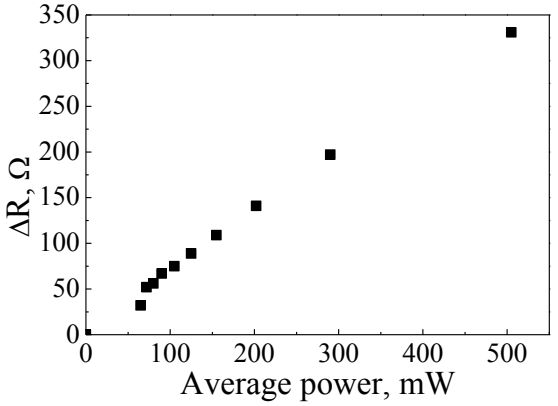

Figure 3.12. Results of measurements the sensor prototype at 94 GHz using magnetron power source.

Using the magnetron power source at 94 GHz the power sensor was tested at high amounts of power up to 500 mW. The output pulse power of the magnetron is 2.2 kW. Measurements were carried out in pulse regime with duty cycles from 3·10-5 to 3·10-4 corresponding to an average power range from 65 to 505 mW. Reference power was measured by HP W8486A power meter with 30 dB attenuation. Results of the measurements are shown in Fig. 3.12.

According to thermal simulations 0.1 mW power applied directly to the metal structure causes approximately 0.28 °C temperature increase, which corresponds to a 0.18 Ω resistance change, which is 1.8 Ω/mW. Measurement results show 0.51 Ω/mW resistance change. The difference can be explained by taking into account that in the thermal simulation the power was evenly dissipated in the structure, however in the power sensor RF heating is not even through the whole structure as it can be seen in Fig. 3.2. In addition, in the power sensor the actual thermal leakage can be higher than that in the simulation; hence the temperature increase of the structure is smaller than in the thermal simulations. Furthermore, due to the surface roughness of the film the square resistance at high frequencies can be higher than that on DC.

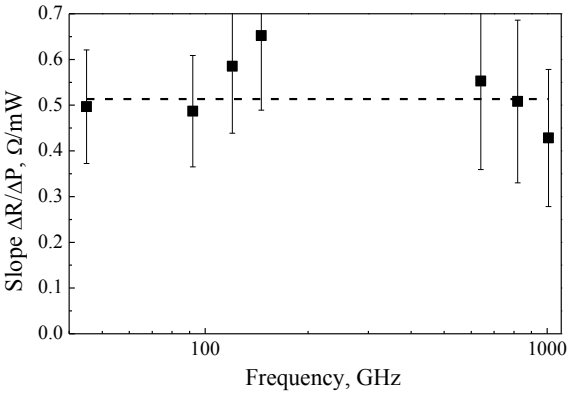

Figure 3.13. The dependence of the slope ΔR/ΔP versus frequency.

The noise equivalent power (NEP) of the power sensor can be estimated by taking into account two main noise sources: phonon noise due to thermal conductance from the bolometer element to the substrate G, and the Johnson noise due to thermal fluctuations in the bolometer resistive element.

The phonon NEP can be expressed as in [33]:

$$\mathrm{NEP}_{\mathrm{ph}}^2 = 4kT^2G, \tag{3.1}$$

where k is the Boltzmann constant, T is the temperature, and G is the thermal conductance from the bolometer element to the substrate. The thermal conductance G can be expressed as in [47]:

$$G = \frac{\partial P}{\partial R} \cdot \frac{\partial R}{\partial T}, \tag{3.2}$$

where $\frac{\partial P}{\partial R}$ is found from the DC measurements of $\Delta R(P)$, and $\frac{\partial R}{\partial T}$ is found from the temperature coefficient of resistance of Cr, resulting in G = 12 mW/K.

The Johnson NEP can be expressed as in [33]:

$$\mathrm{NEP}_{\mathrm{J}}^2 = \frac{4kTR}{R_V^2}, \tag{3.3}$$

where R_V is the voltage responsivity of the power sensor, and it can be expressed as $R_V = I\frac{\Delta R}{\Delta P}$, where I is the bias current through the bolometer during the resistance measurement. At I = 1 mA R_V = 0.5 V/W.

Finally, the total NEP can be expressed as:

$$\mathrm{NEP}^2 = \mathrm{NEP}_{\mathrm{ph}}^2 + \mathrm{NEP}_{\mathrm{J}}^2, \tag{3.4}$$

which results in NEP = 11.5 nW/Hz$^{0.5}$ at I = 1 mA.

4. DRW phase shifter based on a reconfigurable SWCNT HIS

An important component of all the RF, microwave, mm-wave and THz systems is a phase shifter, which is especially interesting when implemented in phased array antennas.

Phase shifters can be analog type or discrete type. Discrete type phase shifters are often realized with switches; they are well developed and show reasonable performance [49-53]. However, implementation of large switching networks and circuitry is inconvenient for, e.g., reflectarrays. Another disadvantage of the switching networks is the discrete characteristics of the phase change since the switching appears between pre-manufactured delay lines.

On the other hand, analog type phase shifters change the phase in a continuous way, and therefore they are more advantageous for beam steering applications. However, the common analog type ferroelectric phase shifters possess high losses at mm-wave frequencies [54].

The prospective candidate for an analog type DRW phase shifter is a high impedance surface (HIS) which is placed on the side of the DRW and change the propagation constant of the wave in the DRW. The HIS is a special case of metamaterials, which are considering a wide range of assembly of structural elements with unique electromagnetic properties [55]. The HIS can consist of electrically small wires, strips, slots, or patches, which determine the surface impedance of the HIS and hence the reflection of incident electromagnetic wave. Around the resonant frequency of HIS the reflection phase of electromagnetic wave is changing from 180° to -180° [56-58]. The resonant frequency of a HIS can be actuated by DC voltage using MEMS patches which can move up and down and change the gap between patches and the ground plane [58-60], hence changing the reflection phase at a given frequency. Placing a HIS on the side of a DRW will result in change of propagating constant and hence a phase shift as shown in [61].

While the existing MEMS technology allows to create reconfigurable transmission lines [62], variable capacitors [63], and reconfigurable metamaterials [60], the resulting structures have a complicated design of movable patches and require high bias voltage to actuate the patches. It is possible to overcome these problems by implementing a carbon nanotube membrane as a movable element in a reconfigurable HIS.

SWCNTs have outstanding electrical and mechanical properties which make them very attractive for future MEMS applications [14, 64]. SWCNTs can be implemented in MEMS devices as individual nanotubes [65], as vertically

aligned forests [66, 67], for reinforcing suspended composite beams [68, 69], or as freestanding films.

Outstanding plasticity and low Young's modulus of the SWCNT films give certain advantages compared with thin films made of traditional materials, such as lower actuating voltages and simpler fabrication process. Recently SWCNT films were implemented in various MEMS devices, such as high frequency switches [50, 70], as mechanical resonators [71], and as vibrating gate electrodes in the field effect transistors [72].

The direct SWCNT deposition technique by dry transfer from the nitrocellulose filter surface [73] reduces the number of fabrication steps and does not require any release procedure, hence improving the repeatability of the fabrication process. Additionally it gives an opportunity to cover large areas which is essentially important for, e.g., creating large reflector antenna surfaces, sensor matrices or large values of capacitance. And finally, it opens the possibility to integrate the SWCNT HIS directly to the surface of a DRW, while in the previous works the HIS had to be fabricated on a separate chip. This chapter reports research work towards such a DRW phase shifter based on a reconfigurable HIS with a movable SWCNT film [V, VI].

4.1 High impedance surfaces

The HIS can consist of a periodic mesh of patches, grids, wires or slots above a ground plane. The resonant frequency of the HIS is determined by dimensions of the structure. The patches and slots are chosen as more advantageous structures in terms of the fabrication process, since it is possible to create movable membranes above a ground plane.

Figure 4.1. Schematic cross-section of a HIS.

A schematic cross-section of a HIS is shown in Fig. 4.1. The metal strips are placed on the dielectric layer with relative permittivity ε_D and thickness h. The relative permittivity of the medium above the HIS is ε_M. The period of the strips is D and the width of the slots between the strips is d.

An approximate model to describe such a HIS was developed in [56] for the normal plane wave incidence. In case of a mesh of slots the model is valid for polarization perpendicular to the slots polarization, and in case of a mesh of square patches the calculations are the same for two perpendicular polarizations of normal incidence due to symmetry.

The impedance of the surface consisting of the mesh of parallel slots placed on the dielectric layer is:

$$Z_S = -j\frac{\eta_{eff}}{2\alpha}, \tag{4.1}$$

where

$$\alpha = \frac{k_{eff} D}{\pi} \ln\left(\frac{1}{\sin\left(\frac{\pi d}{2D}\right)}\right) \tag{4.2}$$

is the mesh parameter, D is the period of the mesh, d is the slot width (see Fig. 4.1). η_{eff} and k_{eff} are the effective wave impedance and the effective wave number, respectively:

$$\eta_{eff} = \sqrt{\frac{\mu_0}{\varepsilon_0 \varepsilon_{eff}}}, \quad \varepsilon_{eff} = \frac{\varepsilon_D + \varepsilon_M}{2}, \quad k_{eff} = k_0 \sqrt{\varepsilon_{eff}}. \tag{4.3}$$

If the mesh is placed above a ground plane at a distance h, then the input impedance of the grounded dielectric layer with permittivity ε_D is:

$$Z_h = j \sqrt{\frac{\mu_0}{\varepsilon_0 \varepsilon_D}} \tan\left(k_0 h \sqrt{\varepsilon_D}\right). \tag{4.4}$$

The impedance of the whole structure is calculated as a parallel connection of Z_S and Z_h:

$$\frac{1}{Z_{tot}} = \frac{1}{Z_S} + \frac{1}{Z_h}. \tag{4.5}$$

Finally, the reflection coefficient is:

$$R = \frac{Z_{tot} - \eta_M}{Z_{tot} + \eta_M}, \tag{4.6}$$

where $\eta_M = \sqrt{\frac{\mu_0}{\varepsilon_0 \varepsilon_M}}$ is the wave impedance of the media above the HIS.

The assumptions of the model are the following: D is smaller than the wavelength, $d \ll D$, and $h > D$. The modification of the formula for $h < D$ is presented in [56]. If the h is smaller than D, the higher-order Floquet modes reflected by the ground plane must be taken into account, resulting in additional coefficient γ added to α in (4.2), and therefore, α must be substituted by $(\alpha + \gamma)$ in (4.1), where

$$\gamma = \frac{k_{eff} D}{\pi} \ln\left(1 - e^{\frac{-4\pi h}{D}}\right). \tag{4.7}$$

This model allows to estimate the initial dimensions of the structure to achieve a resonance at a given frequency. Taking into account the limitations of the fabrication process (further discussed in Section 4.3), possible dimensions of the HIS shown in Fig. 4.1 for a resonance frequency around 100 GHz are the following: $D = 400$ μm, $d = 2$ μm, $h = 4$ μm with $\varepsilon_M = 12$ and $\varepsilon_D = 12$.

These dimensions can be impractical in some cases, for example for a DRW phase shifter it will be advantageous to reduce the period of the slots D to place more elements on the surface of the DRW. To address these issues a multilayer HIS have been studied in [58, 74].

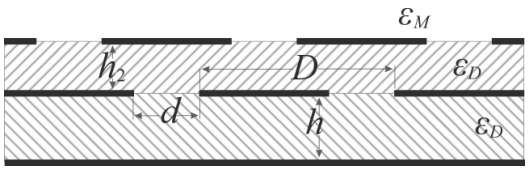

Figure 4.2. A schematic cross section of a two-layer HIS with two grids of the same period.

A schematic image of a two-layer HIS according to [74] in shown in Fig. 4.2. The structure consists of two layers of periodical mesh of slots, separated with dielectric layer of thickness h_2, above the ground plane. The dimensions of two meshes of slots and relative permittivity of two dielectric layers are the same for simplicity.

It is possible to describe a two-layer HIS by introducing a parallel plate capacitance C_{pp} for a unit sell of HIS created between two meshes of slots:

$$C_{pp} = \frac{\varepsilon_0 \varepsilon_D D(D-2d)}{h_2}, \tag{4.8}$$

and the impedance of the two-layer structure can be calculated as a parallel connection of impedances of the two grids of slots Z_{S1} and Z_{S2} (4.1), each calculated with corresponding values of ε_{eff} (4.3), impedance of the grounded dielectric layer Z_h' similar as Z_h in (4.4), but h must be substituted by $h + h_2$, and impedance of the capacitor C_{pp} (4.8):

$$\frac{1}{Z_{two-layer}} = \frac{1}{Z_{S1}} + \frac{1}{Z_{S2}} + \frac{1}{j\omega C_{pp}} + \frac{1}{Z_h'}. \tag{4.9}$$

Introducing a second layer of slots allows to decrease the period of the mesh D, decrease the thickness of the dielectric layer h and decrease the possible values of ε_D, which will be advantageous during fabrication process. Possible dimensions of the HIS shown in Fig. 4.2 for a resonance frequency around 100 GHz are the following: $D = 200$ μm, $d = 4$ μm, $h = 3$ μm, $h_2 = 1$ μm with $\varepsilon_D = 7.5$, and $\varepsilon_M = 12$.

Finally, the resonant frequency of the HIS according to these calculations differs by about 15% from the simulated results. The further discussion of the structure using numerical simulations is presented in Section 4.5.

4.2 Reconfigurable HIS with a SWCNT membrane ground plane

The reflection phase of HIS can be changed by changing one of the dimensions of the structure. The recently emerged MEMS technology allowed to create a tunable HIS with movable patches, i.e. changeable h in Fig. 4.1 or h_2 in Fig. 4.2. However this approach resulted in a complicated and expensive design of MEMS patches, and limitations of the size of the structure due to fabrication process limitations. Another problem of the conventional MEMS varactors is their high actuation voltage (50 V and higher) [63].

It is possible to overcome these problems by using a stationary mesh of slots deposited on a substrate and implementing a SWCNT membrane as a movable ground plane. SWCNTs have outstanding electrical and mechanical properties which make them very attractive for a MEMS technology implementation. While individual SWCNTs possess a high Young's modulus close to 1 TPa [75], the SWCNT networks can have much lower Young's modulus values from 60 MPa to 10 GPa [76]. This can be due to the fact that in a SWCNT network individual tubes are connected to each other with van der Waals forces, which determines the overall elasticity of the film.

The proposed fabrication process for a DRW integrated HIS with a SWCNT membrane is shown in Fig. 4.3. First, the mesh of Au strips are deposited on a high resistivity Si substrate (Fig. 4.3 a)). The period and separation between

the Au strips are corresponding to D and d in (4.2). The maximum period D is not limited by the fabrication process, but it should be smaller than a wavelength according to the HIS model. The minimum slot width d is limited by the lithography resolution. Common optical lithography process has a resolution of 1 μm. It is possible to achieve a smaller resolution, however it requires more expensive process equipment, e.g., e-beam lithography. The relative permittivity of Si substrate is $\varepsilon_M = 11.9$ and it corresponds to ε_M in (4.3). The thickness of the substrate is 500 μm, which allows to cut a DRW of cross-section 1.0 mm × 0.5 mm from the substrate.

Next, the dielectric layer is deposited on top of the first mesh of strips (Fig. 4.3 b)) using plasma enhanced chemical vapor deposition (PECVD) technique. The thickness of the layer corresponds to h_2 in (4.8). The thickness of the layer is limited by the fabrication process to a value from several tens of nanometers to about 4 μm. The common PECVD materials are: amorphous Si (a-Si), SiO_2, and Si_3N_4. The deposition rates of SiO_2 and Si_3N_4 are higher than that of a-Si, and the dielectric constant of Si_3N_4 (ε_r = 7.5) is higher than that of SiO_2 (ε_r = 3.9). Therefore Si_3N_4 is the optimum dielectric in terms of deposition rate and high dielectric constant which results in faster fabrication process and smaller thickness of the layer according to the model (4.8). The dielectric constant of the Si_3N_4 layer corresponds to ε_D in (4.3) and (4.8).

Next the second mesh of Au strips is deposited on top of the Si_3N_4 layer of the same period D and separation d (Fig. 4.3 c)), followed by the deposition of the second layer of Si_3N_4 with the thickness h, which corresponds to h in (4.4) (Fig. 4.3 d)).

The next step is fabrication of the support groove structure for the movable SWCNT ground plane. The properties of the suspended SWCNT film over the groove structure have been studied in [V]. The SWCNT membrane can be suspended between dielectric grooves of width w shown in Fig. 4.3 e) similarly as in [V], however the period of grooves doesn't have to coincide with the metal mesh period D. The aspect ratio of w/h is limited between approximately 8/1 and 20/1 to achieve an optimal control voltage of a movable SWCNT membrane, and it will be further discussed in Section 4.4. The grooves are etched using reactive-ion etching (RIE). The supporting dielectric width s is limited by a ratio $s/h > 2/1$ due to the difficulties in fabrication structures with a high aspect ratio.

Taking into account all mentioned limitations the dimensions of the HIS for a resonance frequency around 100 GHz are the following: $D = 200$ μm, $d = 4$ μm, $h = 3$ μm, $h_2 = 1$ μm, $w = 40$ μm, $s = 10$ μm, with $\varepsilon_D = 7.5$ and $\varepsilon_M = 11.9$.

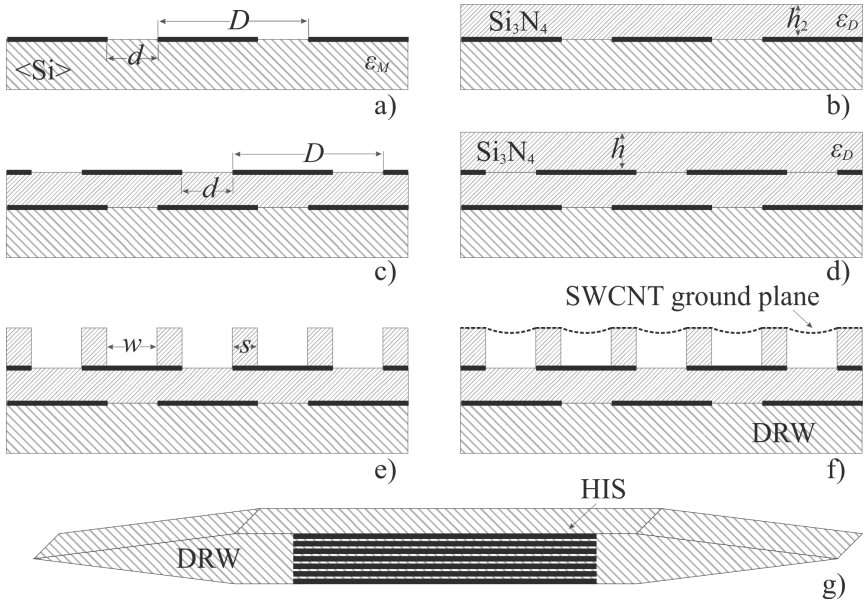

Figure 4.3. Fabrication process of the DRW integrated HIS with a SWCNT membrane.

Finally the substrate is cut by a dicing saw into the form of DRW with cross section of 1.0 mm × 0.5 mm and taperings. The SWCNT film is transferred onto the structure by a direct transfer method from the nitrocellulose filter [73] (Fig. 4.3 f)). The schematic image of a DRW with the HIS fabricated on the side is shown in Fig. 4.3 g).

The resulting HIS has an uneven ground plane, which will result in a resonance frequency shift, however it can be taken into account in numerical simulations.

4.3 Fabrication and testing

The simplified suspended SWCNT membrane structure above the mesh of metal contacts have been fabricated and tested to study the properties and performance of the SWCNT membrane. The SWCNT MEMS were fabricated on a low doped Si substrate (10^4 Ω·cm) to prevent the short-circuit between the SWCNT film and the bottom gold pads. The wafer was covered with a 500 nm layer of Si_3N_4 for insulation. The grooves were patterned using a Microtech LW 405 laser writer lithography on a 1.4 μm thick photoresist AZ 5214E with dimensions $w = 30$ μm, $s = 30$ μm. After the lithography grooves were etched using reactive-ion etching (RIE) with $h = 2$ μm. After the etching, a 24 nm thick Au film was evaporated on the sample covering both the photoresist layer on top and the grooves on the bottom. The following lift-off procedure in acetone resulted in dissolving photoresist and releasing the Au film covering top parts of the structure, while Au film on the bottom parts of grooves remained unaffected. As a result, Au formed a mesh of stripes on the bottom of the grooves with the same dimensions as grooves: $D = 60$ μm, $d = 30$ μm for the

MEMS. The SWCNT film was deposited on the top of the structure with direct transfer method from the nitrocellulose filter after dry transfer [73].

Some nanotubes from the SWCNT film can form a short circuit between the contacts. To avoid it the grooves are filled with nanocellulose aerogel [77]. The nanocellulose aerogel is a soft and flexible porous material. It prevents short circuits between the contacts while it allows the deflection of SWCNT film due to its flexibility and compression. For other samples the nanocellulose aerogel was deposited in the grooves before the deposition of the SWCNT film. After that the SWCNT film was deposited over the structure. Various sets of samples were fabricated and tested: with a freestanding SWCNT film and with a SWCNT film deposited on top of the nanocellulose aerogel. The nanocellulose aerogel has porosity of 98% [77], hence its dielectric constant is close to the dielectric constant of air and the nanocellulose aerogel changes properties of the varactor only mechanically.

A SEM image of the SWCNT film deposited over the groove is shown in Fig. 4.4. In order to visualize the profile a thin 20 μm long stripe was ablated through the SWCNT film using a focused ion beam (FIB). The sample was tilted at 55° while the FIB was perpendicular to the sample surface as it is schematically shown in Fig. 4.4. The FIB ablated both the SWCNT film and an Au film directly under it, while a tilted SEM image allowed to visualize the air gap between the SWCNT and Au films, verifying that the SWCNT film is freestanding.

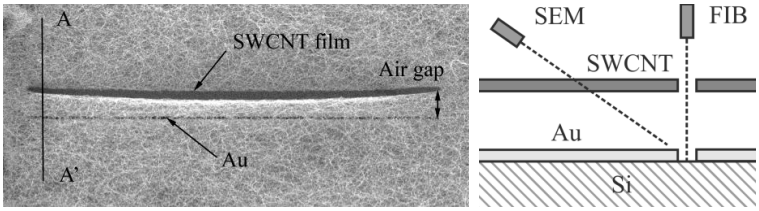

Figure 4.4. Left: SEM image of a suspended SWCNT film after FIB ablation. Right: a schematic A – A' cross-section showing FIB and SEM orientation to the sample.

The SWCNT MEMS were tested at low frequencies using Agilent B1500A semiconductor device analyzer to study the mechanical properties of SWCNT film and the electrical actuation of the gap between the SWCNT membrane and Au strips. The impedance of the structure was measured between the SWCNT membrane and Au strips. The equivalent circuit of the SWCNT MEMS is presented in Fig. 4.5 for the low frequency measurements between the two contacts of the parallel plate capacitor, and it is different from the high frequency surface impedance model described in Section 4.1. The capacitance C is created between the SWCNT film on the top and the Au film on the bottom. The non-capacitive leakage of the current between the SWCNT and Au films is taken into account by introducing the resistance R parallel to the capacitance C. The inductance L_S is taking into account the self-inductance of the SWCNT network.

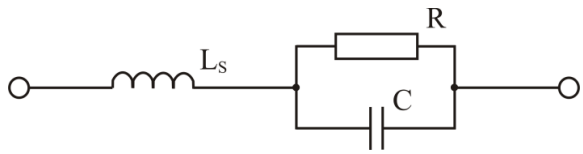

Figure 4.5. SWCNT MEMS circuit model.

Measurements of the device impedance were done over the frequency range of 1 kHz – 1 MHz and then the measured imaginary part of impedance (reactance) was fitted with a calculated reactance for the equivalent circuit shown in Fig. 4.5. This allows us to extract the values of L_S, R and C according to the equivalent circuit model at each bias voltage. The measured and fitted equivalent circuit reactances of the device are shown in Fig. 4.6 at various bias voltages.

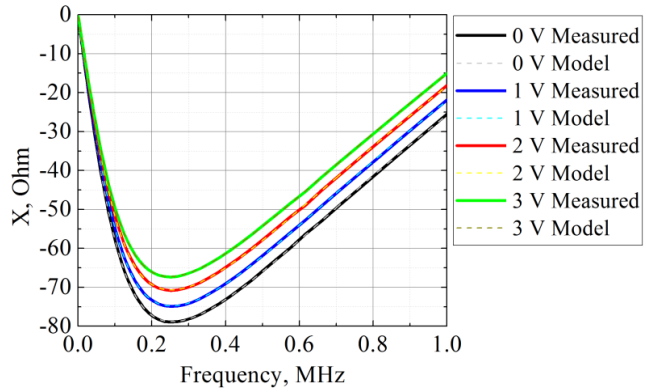

Figure 4.6. Measured (solid lines) and calculated (dashed lines) imaginary part of impedance for different bias voltages.

According to the circuit model the value of inductance stayed almost constant (L_S = 6 µH) independently on the bias voltage, the parallel resistance R is changed in the range of 50 Ω – 80 Ω for the samples without nanocellulose insulation layer and is about 1.3 kΩ with nanocellulose insulation layer. In the case without nanocellulose insulation the resistance R decreased with increasing bias voltage.

The series resistance does not contribute to the reactance and is not included in the circuit model. The value of the series resistance R_S was of the order of 500 Ω for the samples without nanocellulose aerogel and determined by the resistivity of the SWCNT film (≈200 Ω/□).

The value of capacitance at zero bias voltage was C_0 = 3 nF for the sample without nanocellulose and C_0 = 1.8 nF for the sample with nanocellulose. Since the SWCNT films had arbitrary shape and were not covering the whole area of the device, the difference in the values of C is due to different areas of the SWCNT film covering the device.

4.4 SWCNT film deflection model

To extract the parameters of the SWCNT film from the low frequency impedance measurements, the deflection model of the MEMS must be discussed. The cross–section of the structure with a bent SWCNT film is schematically shown in Fig. 4.7. The displacement of the SWCNT film due to the bias voltage can be calculated by equating electrical attraction force and mechanical strain in the SWCNT film.

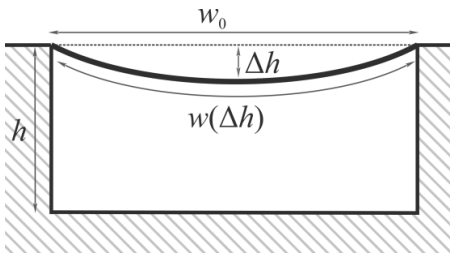

Figure 4.7. Cross section of the bent SWCNT film.

The bias voltage between the SWCNT film and lower contacts create an attraction force:

$$F_C = \frac{1}{2}\frac{\varepsilon_0 A_C V^2}{{h_{eff}}^2(\Delta h)}, \tag{4.10}$$

where ε_0 – permittivity of air, $A_C = w_0 L$ – the area of the plane, w_0 and L – the width and the length of the groove respectively, V – bias voltage, h – depth of the groove, $h_{eff}(\Delta h)$ – mean distance between the SWCNT film and metal contact as a function of maximum film displacement Δh.

The curvature of the SWCNT film increases its length and creates a strain force in the SWCNTs:

$$F_E = E_Y A_{CS}\frac{w(\Delta h) - w_0}{w_0}, \tag{4.11}$$

where E_Y – Young's modulus of the SWCNT film, $A_{CS} = Lt$ – the area of the cross-section of the SWCNT film, t – thickness of the SWCNT film, $w(\Delta h)$ – the length of the bended SWCNT film as a function of Δh. The stiffness of the film is considered negligible. One can find the displacement Δh at given bias voltage V and Young's modulus E_Y by solving equation of $F_C = F_E$ from (4.10) and (4.11):

$$Et\frac{w(\Delta h) - w_0}{w_0} = \frac{1}{2}\frac{\varepsilon_0 w_0 V^2}{{h_{eff}}^2(\Delta h)} \tag{4.12}$$

The following assumptions were taken during the calculations:

1) The profile of the bended SWCNT film is parabolic, which allows to calculate the length $w(\Delta h)$ as a function of Δh.

2) In (4.10) the parallel plate capacitor is considered with the distance between plates $h_{eff}(\Delta h)$.

In contrast to the linear approach, the described method is a more accurate way to calculate the film displacement and to take into account the nonlinear effects in the case of a low density SWCNT film.

4.5 Results

The measured and calculated capacitances of the MEMS varactor *vs*. bias voltage are shown in Fig. 4.8 for two types of the structures: with nanocellulose placed between the SWCNT film and Au pads and without nanocellulose aerogel. The measured capacitance values were extracted from the fitted reactance curves according to the equivalent circuit (see Fig. 4.5 and 4.6). The calculated capacitances were fitted to the measurement results as a function of:

$$C(V) = C_0 \frac{h}{h_{eff}(V)}, \tag{4.13}$$

where C_0 is the capacitance at zero bias voltage. The following constants were taken for calculations in (4.12) and (4.13): t = 30 nm, w_0 = 30 μm, h = 2 μm, and C_0 = 3 nF for the sample without nanocellulose and C_0 = 1.8 nF for the sample with nanocellulose aerogel sublayer.

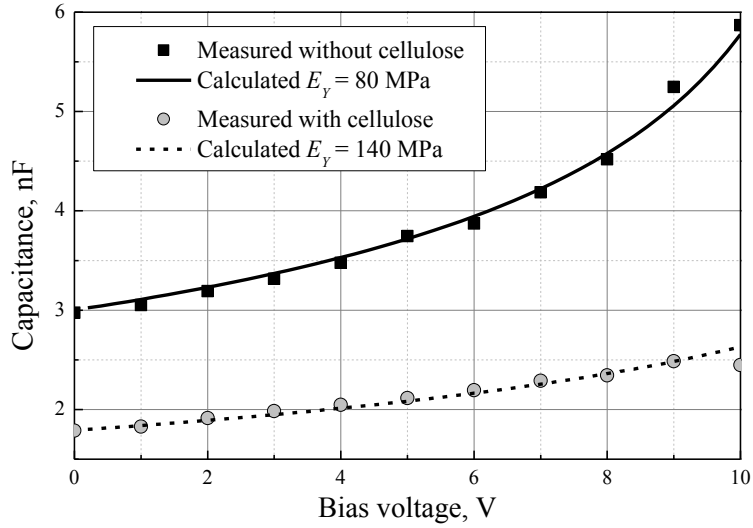

Figure 4.8. Measured and fitted capacitance change of the SWCNT varactor.

The fitting of function (4.13) to the measured results as a function of E_Y and V allows one to extract the value of Young's modulus of E_Y = 80 MPa for the freestanding SWCNT networks without nanocellulose aerogel and E_Y = 140 MPa for the sample of SWCNT networks on nanocellulose aerogel. One can see in Fig. 4.8 that the measured values fit well to the deflection model described with (4.12) and (4.13). The tunability of the capacitance is close to 100%, from 3 nF to 5.8 nF for the sample without nanocellulose filling and 44% from 1.8 to 2.6 nF for the sample with nanocellulose filling at 0 .. 10 V bias voltage. This is 3 times higher tunability than that achieved according to the common linear film deflection model because in the linear deflection model the length increase of the film in not taken into account.

According to the linear deflection model the maximum tunability is 30% [78], after which the pull-in voltage is achieved and the MEMS cantilever is pulled to the bottom of the groove. The pull-in voltage for the SWCNT MEMS

varactor without the nanocellulose aerogel sublayer hasn't been achieved due to decreasing parallel resistance of the device with increasing voltage and short circuit protection of the Agilent B1500A semiconductor device analyzer. From the calculations the pull-in is expected at about 12 V. For the SWCNT MEMS varactor with the nanocellulose aerogel sublayer this sublayer protects the varactor from pull-in.

The obtained Young's modulus of the SWCNT film is E_Y = 80 MPa, that is in very good agreement with previous measurements [76]. With nanocellulose aerogel filling the effective Young's modulus of the system is higher (E_Y = 140 MPa) due to the additional stiffness of nanocellulose aerogel.

The maximum displacement Δh for the sample with E_Y = 80 MPa is 1.60 μm at 10 V bias voltage, hence the gap between the SWCNT film and gold patches changes from 2.00 μm to 0.40 μm. For the sample with E_Y = 140 MPa the gap is changing from 2.00 μm to 0.94 μm.

The length of the film $w(\Delta h)$ (see Fig. 4.7) is 30.23 μm for the displacement Δh = 1.60 μm, and 30.10 μm for the displacement Δh = 1.06 μm, which corresponds to 0.8% and 0.3% length increase respectively. Due to a small relative length increase neither any hysteresis behavior in the capacitance dependence nor any degradation in the varactor performance was noticed.

Knowing the Young's modulus of SWCNT film it is possible to calculate the film deflection for the HIS described in Section 4.2 with w_0 = 40 μm and h = 3 μm according to (4.12). In that case CNT film is displaced to the value Δh = 1.4 μm at 10 V bias voltage.

A double layer HIS structure with a movable membrane suspended over the grooves shown in Fig. 4.3 was simulated in Ansoft HFSS software. The dependences of the reflection phase of the modeled HIS on frequency are shown in Fig. 4.9 for different values of h changing from 3.0 μm to 1.5 μm with steps of 0.1 μm.

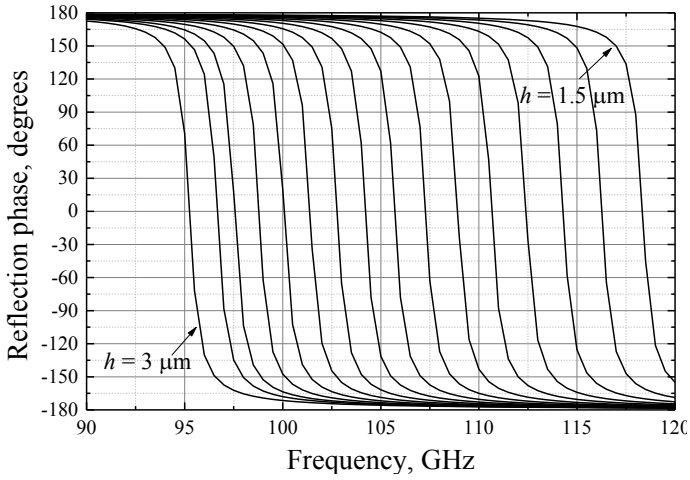

Figure 4.9. Simulated reflection phase from a HIS at different values of h from 3.0 μm to 1.5 μm.

Knowing the Young's modulus of the SWCNT film and the dimensions of the structure it is possible to calculate the reflection phase of the HIS at a given frequency vs. bias voltage. The simulated reflection phase from a HIS vs. bias voltage at 100 GHz is shown in Fig. 4.10.

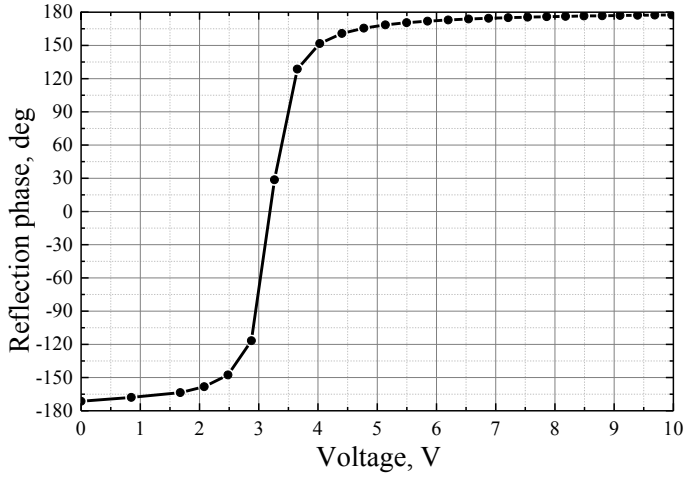

Figure 4.10. Simulated reflection phase from a HIS vs. bias voltage at 100 GHz.

5. Summary of articles

[I] Dielectric rod waveguide antenna for 220 – 325 GHz

A dielectric rod waveguide antenna for 220-325 GHz is presented. Simulations for determining antenna optimal geometry are performed. Measurement results of the radiation pattern are shown and compared with the simulation results at 310 GHz. Matching of the antenna with a metallic waveguide is experimentally studied.

[II] Dielectric rod waveguide antenna at 75 – 1100 GHz

The possibility of using a single dielectric rod waveguide antenna at 75 – 1100 GHz frequency is presented. The simulations of the antenna showed that DRW antenna can be well matched with standard metal waveguides from WR-10 to WR-03 directly and from WR-2 to WR-1 with transitions. The influence of antenna geometry on radiation pattern is studied. The radiation pattern of the antenna is independent of frequency.

[III] Wide band mm and sub-mm wave dielectric rod waveguide antenna

The design of a dielectric rod waveguide (DRW) antenna for frequencies of 75 – 325 GHz is presented. The optimal broadband antenna geometry is determined using numerical simulations. A single DRW antenna is matched with metal waveguides of different sizes for different frequency bands. Measurement results agree very well with the simulation results up to 325 GHz; the gain of the antenna stays nearly constant ($G \approx 10$ dB) over the whole frequency range measured from 75 GHz to 325 GHz (160% relative bandwidth). The upper limit is due to our limited manufacturing capability to produce sharp antenna tips. The return loss of the antenna is better than 15 dB. The radiation patterns are nearly independent of frequency. The 3 dB beamwidth is 50^{o} - 60^{o}, and the 10 dB beamwidth is about 95^{o}. This indicates that the aperture size of this end-fire antenna decreases as a function of frequency, and this observation agrees well with the earlier observation that the phase center of a DRW antenna moves towards the antenna tip as a function of frequency. Also the cross polarization was studied. The cross-polarization level is better than -15 dB at all frequencies.

[IV] Millimeter-wave power sensor based on silicon rod waveguide

A novel type of RF power sensor, based on a metallic structure integrated into an mm-wave DRW made of Si is presented. The metallic structure is employed as a bolometer in the center of DRW. Numerical simulations of temperature distribution are shown. A prototype was tested at frequencies of 45

GHz – 1 THz and a power levels from 0.1 to 500 mW. The power sensor showed the sensitivity of 0.51 Ω/mW resistance change.

[V] Carbon nanotube network varactor

Microelectromechanical system varactors based on a freestanding layer of SWCNT films were designed, fabricated and tested. The freestanding SWCNT film was employed as a movable upper patch in the parallel plate capacitor of the microelectromechanical system. The measurements of the SWCNT varactors show very high tunability, nearly 100%, of the capacitance with a low actuation voltage of 10 V. The functionality of the varactor is improved by implementing a flexible nanocellulose aerogel filling.

[VI] Reconfigurable mm-wave phase shifter based on high impedance surface with carbon nanotube membrane MEMS

A novel phase shifter based on high impedance surface (HIS) with carbon nanotube (SWCNT) membrane MEMS is proposed. The SWCNT MEMS HIS is integrated into a dielectric rod waveguide (DRW) so that the SWCNT membrane acts as a movable ground plane. A presented novel fabrication method of the phase shifter is significantly simpler than those previously used. The device performance is verified through numerical simulations that show a theoretical phase shift of nearly 360° with a 7 V bias voltage applied. In the experimentally demonstrated a SWCNT membrane varactor the distance of the SWCNT membrane and metal patches changed from 2 μm to 0.4 μm with a 10 volt bias.

6. Conclusions and future work

This thesis studies DRW components at sub-THz frequencies. DRWs provide good matching with rectangular metal waveguides and possess low losses. DRWs can be as well used as antennas. The possibility of using a DRW antenna over the 220 – 325 GHz frequency range is shown both numerically and experimentally. The matching and the radiation pattern of the antenna depend on tapering lengths. With both tapering lengths of 6 mm, S_{11} is below -13 dB and the -10 dB beamwidth of the antenna is 75°.

The possibility of using a single DRW antenna over the 75 – 1100 GHz frequency range is shown using numerical simulations. The 8 mm matching taper of the antenna provide good matching with WR-10, WR-08, WR-06, and WR-03 waveguides with S_{11} better than -20 dB, and it is possible to match the antenna with WR-2, WR-1.5 and WR-1 waveguides using a transition. With the transition, S_{11} is better than -17 dB at all frequencies.

Single mode and oversized wideband DRW antennas are compared and they show similar performance indicating that there are no drawbacks using the wideband antenna. The radiation patterns of the wideband DRW antenna are studied using numerical simulations at different radiation tapering lengths. It is shown that a longer tapering provide narrower radiation pattern. The optimal antenna geometry is chosen for fabrication and measurement of the antenna. The wideband DRW antenna has been measured at 75 – 325 GHz. It shows S_{11} better than -15 dB and constant radiation patterns with 95° -10 dB beamwidth and about 10 dB gain over the used frequencies. The results agree well with the simulation data.

The power sensor integrated into DRW has been designed, manufactured and tested. The DRW poser sensor provides good matching with rectangular metal waveguides, has a linear response over a wide range of frequencies, and is capable of measuring high amounts of power. The noise equivalent power of the sensor is NEP = 11.5 nW/Hz$^{0.5}$ at a bias current I = 1 mA.

The SWCNT network film has been implemented as a movable membrane in a parallel plate capacitor. It allows to simplify the fabrication process and reduce the actuation voltage of the MEMS. The measurements of the varactor impedance have been performed at low frequencies, which allows to extract the values of SWCNT film Young's modulus and to estimate the displacement of the film vs. the bias voltage. The measurement results of film stiffness agree with previous observations. In addition it allows to design the mm-wave MEMS HIS which is fabricated directly on the surface of the DRW and provides a phase shift of nearly 360° at low actuation voltage of 7 V.

The future work includes creating wideband DRW antennas integrated with THz sources, phase shifters and power sensors. Additionally, further investigation of SWCNT films properties at sub-THz frequencies is needed. Finally, the DRW waveguides can be fabricated directly on a substrate with integrated devices to create a fully integrated system without using any metal-based transmission lines.

References

[1] P. Siegel, "Terahertz technology," *IEEE Transactions on Microwave Theory and Techniques*, vol. 50, no. 3, pp. 910–928, 2002.

[2] I. Hosako, N. Sekine, M. Patrashin, S. Saito, K. Fukunaga, Y. Kasai, P. Baron, T. Seta, J. Mendrok, S. Ochiai, and H. Yasuda, "At the dawn of a new era in terahertz technology," *Proceedings of the IEEE*, vol. 95, no. 8, pp. 1611–1623, 2007.

[3] T. Kleine-Ostmann and T. Nagatsuma, "A review on terahertz communications research," *Journal of Infrared, Millimeter and Terahertz Waves*, vol. 32, no. 2, pp. 143–171, 2011.

[4] W. Menzel, "Millimeter-wave radar for civil applications," in *European Radar Conference*, Paris, France, September 2010, pp. 261–264.

[5] J. F. Federici, B. Schulkin, F. Huang, D. Gary, R. Barat, F. Oliveira, and D. Zimdars, "THz imaging and sensing for security applications—explosives, weapons and drugs," *Journal of Semiconductor Science and Technology*, vol. 20, no. 7, pp. 266–280, 2005.

[6] J. El Haddad, B. Bousquet, L. Canioni, and P. Mounaix, "Review in terahertz spectral analysis," *Trends in Analytical Chemistry*, vol. 44, pp. 98–105, 2013.

[7] P. H. Siegel, "Terahertz technology in biology and medicine," *IEEE Transactions on Microwave Theory and Techniques*, vol. 52, no. 10, pp. 2438–2447, 2004.

[8] M. Zhadobov, R. Sauleau, V. Vié, M. Himdi, L. Le Coq, and D. Thouroude, "Interactions between 60-GHz millimeter waves and artificial biological membranes: dependence on radiation parameters," *IEEE Transactions on Microwave Theory and Techniques*, vol. 54, no. 6, pp. 2534–2542, 2006.

[9] P. H. Siegel, "THz instruments for space," *IEEE Transactions on Microwave Theory and Techniques*, vol. 55, no. 11, pp. 2957–2965, 2007.

[10] D. Lioubtchenko, S. Tretyakov, and S. Dudorov, *Millimeter-Wave Waveguides*, Kluwer Academic Publishers, 2003.

[11] P. Pousi, *Active and passive dielectric rod waveguide components for millimetre wavelengths*, Ph.D. dissertation, Department of Radio Science and Engineering, School of Science and Technology, Aalto University, Espoo, Finland, 2010.

[12] G. M. Rebeiz, *RF MEMS, Theory, Design, and Technology*, John Wiley & Sons Inc., 2003.

[13] R. Stefanini, M. Chatras, P. Blondy, and G. M. Rebeiz, "Miniature MEMS switches for RF applications," *Journal of Microelectromechanical Systems*, vol. 20, no. 6, pp. 1324–1335, 2011.

[14] X. Zang, Q. Zhou, J. Chang, Y. Liu, and L. Lin, "Graphene and carbon nanotube (CNT) in MEMS/NEMS applications," *Journal of Microelectronic Engineering*, vol. 132, pp. 192–206, 2015.

[15] I. V. Anoshkin, A. G. Nasibulin, Y. Tian, B. Liu, H. Jiang, and E. I. Kauppinen, "Hybrid carbon source for single-walled carbon nanotube synthesis by aerosol CVD method," *Carbon*, vol. 78, pp. 130–136, 2014.

[16] C. F. Moldovan, W. A. Vitale, P. Sharma, L. S. Bernard, and A. M. Ionescu, "Fabrication process and characterization of suspended graphene membranes for RF

NEMS capacitive switches," *Journal of Microelectronic Engineering*, vol. 145, pp. 5–8, 2015.

[17] C. Yeh and F. Shimabukuro, *The Essence of Dielectric Waveguides*, Springer, 2008.

[18] S. Kobayashi, R. Lampe, N. Deo, and R. Mittra, "Dielectric antennas for millimeter-wave applications," in *IEEE MTT-S International Microwave Symposium Digest*, 1979, pp. 566-568.

[19] S. Kobayashi, R. Lampe, R. Mittra, and S. Ray, "Dielectric rod leaky-wave antennas for millimeter-wave applications," *IEEE Transactions on Antennas and Propagation*, vol. 29, no. 5, pp. 822–824, 1981.

[20] S. Kobayashi, R. Mittra, and R. Lampe, "Dielectric tapered rod antennas for millimeter-wave applications," *IEEE Transactions on Antennas and Propagation*, vol. 30, no. 1, pp. 54–58, 1982.

[21] E. A. J. Marcatili, "Dielectric rectangular waveguide and directional coupler for integrated optics," *Bell System Technical Journal*, vol. 48, pp. 2071–2102, 1969.

[22] J. E. Goell, "A circular-harmonic computer analysis of rectangular dielectric waveguides," *Bell System Technical Journal*, vol. 48, pp. 2133–2160, 1969.

[23] J. P. Pousi, D. V. Lioubtchenko, S. N. Dudorov, J. A. Mallat, and A. V. Räisänen, "High permittivity dielectric rod waveguide antenna for 110-150 GHz," in *Proc. of the First European Conference on Antennas and Propagation*, Nice, France, 6-10 November, 2006.

[24] A. Rivera-Lavado, S. Preu, L. E. García-Muñoz, A. Generalov, J. Montero-de-Paz, G. Döhler, D. Lioubtchenko, S. Malzer, A. V. Räisänen, and D. Segovia-Vargas, "Dielectric rod waveguide antenna as THz emitter for photomixing devices," *IEEE Transactions on Antennas and Propagation*, vol. 63, no. 3, pp. 882–890, 2015.

[25] B. Andres-Garcia, E. Garcia-Munoz, S. Bauerschmidt, S. Preu, S. Malzer, G. H. Döhler, W. Lijun D. Segovia-Vargas, "Gain enhancement by dielectric horns in the terahertz band," *IEEE Transactions on Antennas and Propagation,* vol. 59, no. 9, pp. 3164–3170, 2011.

[26] J.A. Paul and Y.W. Chang, "Millimeter-wave image-guide integrated passive devices," *IEEE Transactions on Microwave Theory and Techniques*, vol. 26, no. 10, 1978.

[27] A. Marconnet, M. He, S. Sengele, S. Ho, H. Jiang, N. Ferrier, D. van der Weide, and J. Booske, "Micromachined step-tapered high frequency waveguide inserts and antennas," *IEEE International Vacuum Electronics Conference*, 22-24 April, 2008, pp. 22–23.

[28] S. M. Hanham, T. S. Bird, A. D. Hellicar, and R. A. Minasian, "Evolved-profile dielectric rod antennas," *IEEE Transactions on Antennas and Propagation*, vol. 59, no. 4, pp. 1113–1122, 2011.

[29] T. Ando, I. Ohba, S. Numata, J. Yamauchi, and H. Nakano, "Linearly and curvilinearly tapered cylindrical-dielectric-rod antennas," *IEEE Transactions on Antennas and Propagation*, vol. 53, no. 9, pp. 2827–2833, 2005.

[30] Y. T. Lo and S. W. Lee, *Antenna Handbook*, Springer, 1993.

[31] P. Padilla, P. Pousi, A. Tamminen, J. Mallat, J. Ala-Laurinaho, M. Sierra-Castañer, and A. Räisänen, "Mm-wave DRW antenna phase centre determination: comparison of different experimental methods," *IEEE Transactions on Antennas and Propagation*, vol. 59, no. 8, pp. 2806–2812, 2011.

[32] A. D. Yaghjian, "Approximate formulas for the far field and gain of open-ended rectangular waveguide," *IEEE Transactions on Antennas and Propagation*, vol. 32, no. 4, pp. 378–384, April 1984.

[33] P. L. Richards, “Bolometers for infrared and millimeter waves,” *J. Appl. Phys*, vol. 76, no. 1, pp. 1–24, 1994.

[34] S. Cherednichenko, A. Hammar, S. Bevilacqua, V. Drakinskiy, J. Stake, and A. Kalabukhov, “A Room Temperature Bolometer for Terahertz Coherent and Incoherent Detection,” *IEEE Transactions on Terahertz Science and Technology*, vol. 1, no. 2, pp 395–402, 2011.

[35] A. Luukanen, M. M. Leivo, A. Rautiainen, M. Grönholm, H. Toivanen, L. Grönberg, P. Helistö, A. Mäyrä, M. Aikio, and E. N. Grossman, “Applications of superconducting bolometers in security imaging,” *Journal of Physics: Conference Series*, vol. 400, 052018, 2012.

[36] A. Luukanen, E. N. Grossman, A. J. Miller, P. Helistö, J. S. Penttilä, H. Sipola, and H. Seppä, “An ultra-low noise superconducting antenna-coupled microbolometer with a room-temperature read-out,” *IEEE Microwave and Wireless Components Letters*, vol. 16, no. 8, pp. 464–466, 2006.

[37] V. Tamošiūnas, Ž. Kancleris, M. Dagys, R. Simniškis, and F.J. Agee, “Resistive sensor for short high-power microwave pulse measurement in millimeter wave range,” *Acta Physica Polonica A*, vol. 107, no. 2, pp. 420–424, 2005.

[38] P. J. Meier, “Integrated fin-line millimeter components,” *IEEE Transactions on Microwave Theory and Techniques*, vol. 22, no. 12, pp. 1209–1216, 1974.

[39] J. P. Pousi, D. V. Lioubtchenko, S. N. Dudorov, and A. V. Räisänen, “High permittivity dielectric rod waveguide as an antenna array element for millimeter waves,” *IEEE Transactions on Antennas and Propagation*, vol. 58, pp. 714–719, 2010.

[40] D. P. Neikirk, W. W. Lam, and D. B. Rutledge, “Far-infrared microbolometer detectors,” *Int. J . Infrared and Millimeter Waves*, vol. 5, pp. 245–476, 1984.

[41] A. J. Miller, A. Luukanen, and E. N. Grossman, “Micromachined antenna-coupled uncooled microbolometers for terahertz imaging arrays,” in *Proc. of SPIE*, vol. 5411, pp. 18–24, 2004.

[42] C. C. Ling, J. C. Landry, H. Davee, G. Chin, and G. M. Rebeiz, “Large area bolometers for THz power measurements,” *IEEE Transactions on Microwave Theory and Techniques*, vol. 42, no. 4, pp. 758–760, 1994.

[43] V. Milanovic, M. Gaitan, E. D. Bowen, N. H. Tea, and M. E. Zaghloul, “Thermoelectric power sensor for microwave applications by commercial CMOS fabrication,” *IEEE Electron Device Letters*, vol. 18, no. 9, pp. 450–452, 1997.

[44] A. V. Timofeev, V. Vesterinen, P. Helistö, L. Grönberg, J. Hassel, and A. Luukanen, “Submillimeterwave kinetic inductance bolometers on freestanding nanomembranes,” *Supercond. Sci. Technol.*, vol. 24, 025002, 2014.

[45] T. May, V. Zakosarenko, E. Kreysa, W. Esch, S. Anders, H.-P. Gemuend, E. Heinz, and H.-G. Meyer, “Design, realization, and characteristics of a transition edge bolometer for submillimeter wave astronomy,” *Review of Scientific Instruments*, vol. 83, 114502, 2012.

[46] R. Appleby and H. B. Wallace, “Standoff detection of weapons and contraband in the 100 GHz to 1 THz region,” *IEEE Transactions on Antennas and Propagation*, vol. 55, no. 11, pp. 2944–2956, 2007.

[47] A. Hammar, S. Cherednichenko, S. Bevilacqua, V. Drakinskiy, and J. Stake, “Terahertz direct detection in $YBa_2Cu_3O_7$ microbolometers,” *IEEE Transactions on Terahertz Science and Technology*, vol. 1, no. 2, pp 390–394, 2011.

[48] M. Kroug, S . Cherednichenko, H. Merkel, E. Kollberg, B. Voronov, G. Gol'tsman, H.W. Huebers, and H. Richter, “NbN hot electron bolometric mixers for terahertz receivers,” *IEEE Transactions on Applied Superconductivity*, vol. 11, no. 1, pp. 962–965, 2001.

[49] N. Somjit, G. Stemme, and J. Oberhammer, “Binary-coded 4.25-bit W-band monocrystalline–silicon MEMS multistage dielectric-block phase shifters,” *IEEE Transactions on Microwave Theory and Techniques*, vol. 57, no. 11, pp. 2834–2840, 2009.

[50] D. Acquaviva, A. Arun, S. Esconjauregui, D. Bouvet, J. Robertson, R. Smajda, A. Magrez, L. Forro, and A. M. Ionescu, “Capacitive nanoelectromechanical switch based on suspended carbon nanotube array,” *Applied Physics Letters*, no. 97, 233508, 2010.

[51] Z. Baghchehsaraei, A. Vorobyov, J. Åberg, E. Fourn, R. Sauleau, and J. Oberhammer, “Waveguide-integrated MEMS-based phase shifter for phased array antenna,” *IET Microwaves, Antennas & Propagation*, vol. 8, no. 4, pp. 235–243, 2014.

[52] Y. Aouial, S. Méric, O. Lafond, and M. Himdi, “Passive millimeter wave imaging: 2D sparse array optimization for low cost system architecture,” in *Proc. of the 6th European Conference on Antennas and Propagation*, Prague, Czech Republic, 26-30 Mar. 2012, pp. 3421–3425.

[53] Y. Aouial, S. Méric, O. Lafond, and M. Himdi, “Synthesis of sparse planar arrays for passive imaging systems based on switch submatrix,” *IEEE Geoscience and Remote Sensing Letters*, vol. 9, no. 6, pp. 1007–1011, 2012.

[54] A. S. Tatarenko and G. Srinivasan, “A strain engineered voltage tunable millimeter-wave ferrite phase shifter,” *Microwave and Optical Technology Letters*, vol. 53, no. 2, pp. 261–264, 2011.

[55] S. Tretyakov, *Analytical Modeling in Applied Electromagnetics*, Artech House, Boston, 2003.

[56] S. A. Tretyakov and C. R. Simovski, “Dynamic model of artificial reactive impedance surfaces,” *Journal of Electromagnetic Waves and Applications*, no. 17, pp 131–145, 2003.

[57] D. Sievenpiper, *High-impedance Electromagnetic Surfaces*, Ph.D. dissertation, Dept. Elect. Eng., University of California at Los Angeles, CA, 1999.

[58] D. Chicherin, *Studies on microelectromechanically tuneable high-impedance surface for millimetre wave beam steering*, Department of Radio Science and Engineering, School of Electrical Engineering, Aalto University, Espoo, Finland, 2011.

[59] D. Chicherin, M. Sterner, D. Lioubtchenko, J. Oberhammer, A.V. Räisänen, “Analog-type millimetre wave phase shifters based on MEMS tunable high-impedance surface and dielectric rod waveguide,” *International Journal of Microwave and Wireless Technologies,* vol. 3, no. 5, pp. 533–538, 2011.

[60] J. P. Turpin, J. A. Bossard, K. L. Morgan, D. H. Werner, and P. L. Werner, “Reconfigurable and tunable metamaterials: a review of the theory and applications,” *International Journal of Antennas and Propagation*, vol. 2014, 429837, 2014.

[61] D. Chicherin, M. Sterner, J. Oberhammer, S. Dudorov, D. Lioubtchenko, A.J. Niskanen, V. Ovchinnikov, and A.V. Räisänen, “MEMS based high-impedance surface for millimetre wave dielectric rod waveguide phase shifter,” in *Proc. of the 40th European Microwave Conf.*, Paris, France, September 28-30, 2010, pp. 950–953.

[62] U. Shah, M. Sterner, and J. Oberhammer, “Multi-position RF MEMS tunable capacitors using laterally moving sidewalls of 3-D micromachined transmission lines,” *IEEE Transactions on Microwave Theory and Techniques*, vol. 61, no. 6, pp. 2340–2352, 2013.

[63] C-H. Han, D.-H. Choi, and J.-B. Yoon, “Parallel-plate MEMS variable capacitor with superior linearity and large tuning ratio using a levering structure,” *Journal of Microelectromechanical Systems*, vol. 20, no. 6, pp. 1345–1354, 2011.

[64] Y. Hayamizu, T. Yamada, K. Mizuno, R. C. Davis, D. N. Futaba, M. Yumura, and K. Hata, “Integrated three-dimensional microelectromechanical devices from processable carbon nanotube wafers,” *Nature Nanotechnology*, vol. 3, 289–294, 2008.

[65] Y. Hanein, “Carbon nanotube integration into MEMS devices,” *Phys. Status Solidi B*, vol. 247, pp. 2635–2640, 2010.

[66] A. Arun, H. Le Poche, T. Idda, D. Acquaviva, M. F.-B. Badia, P. Pantigny, P. Salet, and A. M. Ionescu, “Tunable MEMS capacitors using vertical carbon nanotube arrays grown on metal lines,” *Nanotechnology*, vol. 22, 025203, 2011.

[67] M. Meyyappan, “A review of plasma enhanced chemical vapour deposition of carbon nanotubes,” *Journal of Physics D: Applied Physics*, vol. 42, 213001, 2009.

[68] D. Lee and T. Cui, “Suspended carbon nanotube nanocomposite beams with a high mechanical strength via layer-by-layer nano-self-assembly,” *Nanotechnology*, vol. 22, 165601, 2011.

[69] A. G. Nasibulin, A. Ollikainen, A. S. Anisimov, D. P. Brown, P. V. Pikhitsa, S. Holopainen, J. S. Penttilä, P. Helistö, J. Ruokolainen, M. Choi, and E. I. Kauppinen, “Integration of single-walled carbon nanotubes into polymer films by thermo-compression,” *Chemical Engineering Journal*, vol. 136, pp. 409–413, 2008.

[70] A. B. Kaul, E. W. Wong, L. Epp, and B. D. Hunt, “Electromechanical carbon nanotube switches for high-frequency applications,” *Nano Letters*, vol. 6, no. 5, pp. 942–947, 2006.

[71] A. K. Hüttel, G. A. Steele, B. Witkamp, M. Poot, L. P. Kouwenhoven, and H. S. J. van der Zant, “Carbon nanotubes as nltrahigh quality factor mechanical resonators,” *Nano Letters*, vol. 9, no. 7, pp. 2547–2552, 2009.

[72] A. Arun, S. Campidelli, A. Filoramo, V. Derycke, P. Salet, A. M. Ionescu, and M. F. Goffman, “SWNT array resonant gate MOS transistor,” *Nanotechnology*, vol. 22, 055204, 2011.

[73] A. Kaskela, A. G. Nasibulin, M. Y. Timmermans, B. Aitchison, A. Papadimitratos, Y. Tian, Z. Zhu, H. Jiang, D. P. Brown, A. Zakhidov, and E. I. Kauppinen, “Aerosol synthesized SWCNT networks with tuneable conductivity and transparency by dry transfer technique” *Nano Letters*, vol. 10, no. 11, pp. 4349–4355, 2010.

[74] D. Chicherin, S. Dudorov, D. Lioubtchenko, V. Ovchinnikov, and A.V. Räisänen, “Characterisation and measurements of a multilayer highimpedance surface at W-band,” in *Proc. of the 1st International Congress on Advanced Electromagnetic Materials in Microwave and Optics*, Rome, Italy, October 22-26, 2007, pp. 891–894.

[75] N. Yao and V. Lordi, “Young’s modulus of single-walled carbon nanotubes,” *Journal of Applied Physics*, vol. 84, no. 4, pp. 1939–1943, 1998.

[76] A. G. Nasibulin, A. Kaskela, K. Mustonen, A. S. Anisimov, V. Ruiz, S. Kivistö, S. Rackauskas, M. Y. Timmermans, M. Pudas, B. Aitchison, M. Kauppinen, D. P. Brown, O. G. Okhotnikov, and E. I. Kauppinen, “ Multifunctional freestanding single-walled carbon nanotube films,” *ACS Nano*, vol. 5, no. 4, pp. 3214–3221, 2011.

[77] M. Pääkkö, J. Vapaavuori, R. Silvennoinen, H. Kosonen, M. Ankerfors,Tom Lindström, L. A. Berglundc, and O. Ikkala, “Long and entangled native cellulose

I nanofibers allow flexible aerogels and hierarchically porous templates for functionalities," *Soft Matter*, vol. 4, no. 12, pp. 2492–2499, 2008.

[78] G. M. Rebeiz, *RF MEMS: Theory, Design, and Technology*, John Wiley & Sons, Inc., Hoboken, New Jersey, 2003.

This thesis is focused on the development of dielectric rod waveguide (DRW) components at sub-THz frequencies. DRWs proved themselves as low loss transmission lines at sub-millimeter wave and THz frequencies; they can be well matched with rectangular metal waveguides, and also used as antennas. In the first part of this thesis the narrow band and wide band mm wave DRW antennas were designed, manufactured and tested. In the second part of this thesis the bolometric power sensor integrated into DRW was designed, manufactured and tested at frequencies 75 – 1010 GHz. In the third part of this thesis the microelectromechanical system (MEMS) tunable HIS was developed for integration on to the surface of a DRW using suspended carbon nanotube (SWCNT) film as a movable element of the HIS.

Aalto-DD 99/2015

ISBN 978-952-60-6297-6 (printed)
ISBN 978-952-60-6298-3 (pdf)
ISSN-L 1799-4934
ISSN 1799-4934 (printed)
ISSN 1799-4942 (pdf)

Aalto University
School of Electrical Engineering
Department of Radio Science and Engineering
www.aalto.fi

BUSINESS + ECONOMY

ART + DESIGN + ARCHITECTURE

SCIENCE + TECHNOLOGY

CROSSOVER

DOCTORAL DISSERTATIONS